Main eddy vertical structures observed in the four major Eastern Boundary Upwelling Systems

Cori Pegliasco, Alexis Chaigneau, Rosemary Morrow

AGU PUBLICATIONS

JGR

Journal of Geophysical Research: Oceans

RESEARCH ARTICLE

10.1002/2015JC010950

Key Points:
- The main eddy characteristics at the sea-surface are described in each EBUS
- We depict the main eddy vertical structures that coexist in each EBUS
- The proportion of surface and subsurface eddies is provided for each EBUS

Correspondence to:
Cori Pegliasco
cori.pegliasco@legos.obs-mip.fr

Citation:
Pegliasco, C., A. Chaigneau, and R. Morrow (2015), Main eddy vertical structures observed in the four major Eastern Boundary Upwelling Systems, *J. Geophys. Res. Oceans*, *120*, 6008–6033, doi:10.1002/2015JC010950.

Received 30 APR 2015
Accepted 12 AUG 2015
Accepted article online 14 AUG 2015
Published online 5 SEP 2015

Main eddy vertical structures observed in the four major Eastern Boundary Upwelling Systems

Cori Pegliasco[1], Alexis Chaigneau[1,2], and Rosemary Morrow[1]

[1]Laboratoire d'Etudes en Géophysique et Océanographie Spatiales, UMR CNRS, Université Paul Sabatier, CNES, IRD, Toulouse, France, [2]Instituto del MAR de PErú, Callao, Perú

Abstract In the four major Eastern Boundary Upwelling Systems (EBUS), mesoscale eddies are known to modulate the biological productivity and transport near-coastal seawater properties toward the offshore ocean, however little is known about their main characteristics and vertical structure. This study combines 10 years of satellite-altimetry data and Argo float profiles of temperature and salinity, and our main goals are (i) to describe the main surface characteristics of long-lived eddies formed in each EBUS and their evolution, and (ii) to depict the main vertical structure of the eddy-types that coexist in these regions. A clustering analysis of the Argo profiles surfacing within the long-lived eddies of each EBUS allows us to determine the proportion of surface and subsurface-intensified eddies in each region, and to describe their vertical structure in terms of temperature, salinity and dynamic height anomalies. In the Peru-Chile Upwelling System, 55% of the sampled anticyclonic eddies (AEs) have subsurface-intensified maximum temperature and salinity anomalies below the seasonal pycnocline, whereas 88% of the cyclonic eddies (CEs) are surface-intensified. In the California Upwelling System, only 30% of the AEs are subsurface-intensified and all of the CEs show maximum anomalies above the pycnocline. In the Canary Upwelling System, ∼40% of the AEs and ∼60% of the CEs are subsurface-intensified with maximum anomalies extending down to 800 m depth. Finally, the Benguela Upwelling System tends to generate ∼40–50% of weak surface-intensified eddies and ∼50–60% of much stronger subsurface-intensified eddies with a clear geographical distribution. The mechanisms involved in the observed eddy vertical shapes are discussed.

1. Introduction

The four major Eastern Boundary Upwelling Systems (EBUS), namely the Peru-Chile and California Upwelling Systems (PCUS and CALUS, respectively) in the Pacific Ocean, and the Canary and Benguela Upwelling Systems (CANUS and BENUS, respectively) in the Atlantic Ocean, share similar characteristics. First, due to the presence of permanent large-scale atmospheric subtropical anticyclones above the four ocean basins, the winds blow parallel to the coasts toward the equator [*Bakun and Nelson*, 1991; *Tomczak and Godfrey*, 1994]. Under the action of these winds, the four EBUS are characterized by an offshore Ekman transport of the near-surface water and the upwelling of relatively cold and nutrient-enriched deep water along the coast, promoting an intense biological productivity in the near-surface layers [*Carr and Kearns*, 2003; *Chavez and Messié*, 2009]. Indeed, these four regions, which cover only ∼1% of the total ocean area of the world, support large industrial fisheries and represent around 20% of the global fish catch [*Pauly and Christensen*, 1995; *Fréon et al.*, 2009].

Second, the four EBUS exhibit similar large-scale dynamics with the presence of near-coastal equatorward currents that carry relatively fresh and cold water in the surface layers from higher latitudes [*Strub et al.*, 1998, 2013; *Batteen et al.*, 2000; *Hardman-Mountford et al.*, 2003; *Machín et al.*, 2006]. This surface circulation is mainly wind-forced, but also reinforced, through geostrophic adjustment, by the cross-shore temperature (and density) gradients that separate relatively cold upwelled coastal water from warm offshore water. In contrast, in subsurface layers, the four EBUS encompass relatively strong undercurrents that flow poleward along the continental slope, carrying relatively warm and salty waters of equatorial origin [*Silva and Neshyba*, 1979; *Mittelstaedt*, 1983; *Barton et al.*, 1998; *Garfield et al.*, 1999; *Pierce et al.*, 2000; *Gordon*, 2003; *Shillington et al.*, 2006; *Hutchings et al.*, 2009; *Montes et al.*, 2010].

Third, both the velocity shear of the near coastal current systems and the mean Ekman circulation that transports relatively denser coastal water above lighter offshore waters, lead to the formation of instabilities.

In the four EBUS, these instabilities favor the generation of mesoscale eddies that are mainly formed near the coast and propagates mostly westward toward the interior of subtropical gyres, [*Morrow et al*., 2004; *Chaigneau et al*., 2009; *Chelton et al*., 2011]. These nonlinear mesoscale eddies trap water into their cores and participate to the general mixing and redistribution of physical and bio-geochemical properties from the coastal regions to the open ocean [*Logerwell and Smith*, 2001; *Barton and Arístegui*, 2004; *Rubio et al*., 2009; *Morales et al*., 2012; *Dong et al*., 2014]. Along their paths, they can also modulate the bio-geochemistry and ocean productivity [*Correa-Ramirez et al*., 2007; *Marchesiello and Estrade*, 2007; *Gruber et al*., 2011; *Stramma et al*., 2013; *Mahadevan*, 2014] but also impact the overlaying atmosphere interactions affecting heat fluxes at the sea-air interface, winds, cloud cover and precipitations [*Morrow and Le Traon*, 2012; *Frenger et al*., 2013; *Mahadevan*, 2014; *Villas Bôas et al*., 2015].

The general physical properties of mesoscale eddies have been extensively described within each of the four EBUS in particular from sea-level anomaly (SLA) maps acquired from multimissions altimeters [*Chaigneau et al*., 2008; *Rubio et al*., 2009; *Sangrà et al*., 2009; *Kurian et al*., 2011], and from numerical simulations [e.g., *Colas et al*., 2012; *Kurian et al*., 2011; *Batteen et al*., 2000; *Rubio et al*., 2009]. Comparisons of eddy dynamics between EBUS have also been performed [e.g., *Morrow et al*., 2004; *Marchesiello and Estrade*, 2007; *Capet et al*., 2008, 2014; *Chaigneau et al*., 2009]. Although the main eddy characteristics depend on their region of formation and the considered latitude, the four EBUS eddies have typical radii of 50–150 km and amplitudes of 5–10 cm, and propagate westward with speeds of 5–10 $cm.s^{-1}$ [e.g., *Chaigneau et al*., 2009; *Capet et al*., 2014]. Compared to the surface eddy characteristics, the vertical structure of the eddies formed in the 4 EBUS has been poorly documented. The few studies describing the vertical distribution of the temperature and salinity fields inside eddies in the EBUS are mainly based on individual eddies, sampled during specific cruises and in restricted areas [e.g., *De Ruijter et al*. [1999], *Garzoli et al*. [1999], *Froyland et al*. [2012] for the BENUS; *Huyer et al*. [1998], *Kurian et al*. [2011], *Dong et al*. [2012] for the CALUS; *Paillet et al*. [2002], *Sangrà et al*. [2007] for the CANUS; *Holte et al*. [2013], *Hormazabal et al*. [2013] for the PCUS]. However, by merging satellite altimetry data and Argo float profiles, *Chaigneau et al*. [2011] have been able to reconstruct the mean thermohaline vertical structure of composite eddies in the PCUS. On average in this EBUS, relatively warm and salty anticyclonic eddies are mainly subsurface intensified, whereas cold and fresh cyclonic eddies are surface-intensified [*Johnson and McTaggart*, 2010; *Chaigneau et al*., 2011; *Colas et al*., 2012]. The vertical shift of the eddy core was attributed to the mechanisms involved in the eddy generation, suggesting that cyclonic eddies (CEs) are formed by instabilities of the equatorward near-coastal currents whereas subthermocline anticyclonic eddies (AEs) are likely shed by the subsurface poleward Peru-Chile Undercurrent [*Johnson and McTaggart*, 2010; *Chaigneau et al*., 2011; *Colas et al*., 2012].

Given the opportunity to investigate the subsurface physical characteristics of the eddies from Argo float data [*Chaigneau et al*., 2011; *Liu et al*., 2012; *Yang et al*., 2013; *Castelao*, 2014], we analyze, classify and compare the eddy vertical structures in the 4 EBUS from altimetry maps and Argo profiles. In particular, as the 4 EBUS share similar large-scale dynamics, we aim to examine whether the mean eddy vertical thermohaline structures are also similar in the 4 EBUS. Applying a hierarchical classification method on the Argo float profiles, we aim to determine and quantify, within each EBUS, the distinct eddy-types that coexist (e.g., surface or subsurface-intensified cores). The temporal evolution of some of the eddy characteristics and vertical structure is also examined.

2. Data and Methods

In order to study the eddy vertical structure in the 4 EBUS, two main data sets are used: altimetric sea level anomaly maps to automatically detect mesoscale eddies at the sea-surface, and vertical temperature and salinity profiles acquired by Argo floats to examine the vertical distribution of these parameters within the detected eddies.

2.1. Sea-Level Altimetry Maps and Eddy Tracking Algorithm

The presence and position of mesoscale eddies in the four EBUS were determined by analyzing daily sea-level anomaly (SLA) maps produced by Ssalto/Duacs and distributed by CLS (Space Oceanography Division, Toulouse, France: http://www.aviso.oceanobs.com). This gridded multimissions altimeter product, computed relative to a 7 year mean (1993–1999), was extracted from January 2000 to December 2010 to match the Argo floats' availability. The daily SLA maps we used were distributed at the end of 2013, before the

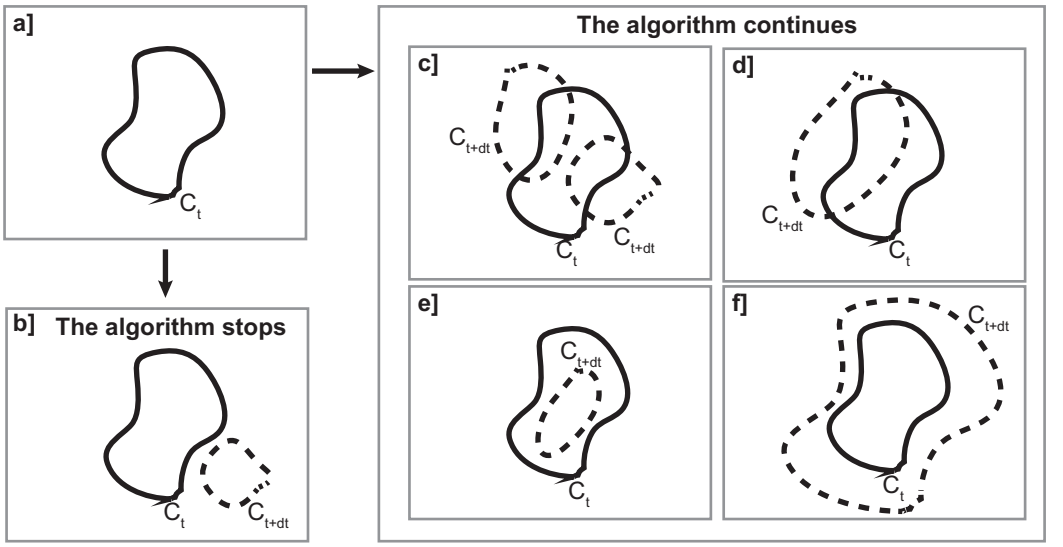

Figure 1. Illustration of the eddy tracking algorithm. (a) Black solid contours represent a given eddy edge (C_t) at time t whereas black dashed contours represent eddy edges (C_{t+dt}) at time $t+dt$. Several cases are presented: (b) no intersection between eddies at time $t+dt$ and C_t and the eddy tracking is stopped; (c) several eddies at $t+dt$ intersect C_t and the eddy-tracking algorithm uses a cost function to determine the one most similar to C_t; (d) only one eddy at $t+dt$ intersects C_t; (e) C_{t+dt} is included within C_t; (f) C_t is included within C_{t+dt}.

more recent DUACS 2014 version that is computed relative to a 20 year mean. Although the reference period and interpolation scales differ between both products, a similar data processing procedure is used to merge and interpolate alongtrack SLA data on a daily Cartesian grid of 0.25 °× 0.25 °spatial resolution.

In a first stage, mesoscale eddies were detected on each SLA map using the algorithm initially developed by *Chaigneau et al*. [2008] and slightly modified by *Chaigneau et al*. [2009]. This algorithm detects eddy centers corresponding to local SLA extrema (minima for CEs and maxima for AEs). Then, for each detected eddy center, the algorithm searches for the eddy edge that corresponds to the outermost closed SLA contour encircling only the considered center. This eddy detection method detects fewer false eddies than other classically used methods [*Chaigneau et al*., 2008; *Souza et al*., 2011; *Yi et al*., 2014] and is similar to the one used by *Chelton et al*. [2011] to study the main eddy characteristics at global scale.

In a second stage, in order to monitor the evolution of mesoscale eddies along their pathways in the four EBUS, each vortex was tracked from the time of its appearance to its dissipation. First, the tracking algorithm classified eddies according to their polarity (cyclonic or anticyclonic). Second, for each eddy edge identified at time t and delimited by a contour C_t (Figure 1a), the algorithm searches at time $t+dt$ (dt = 1 day) for any eddy edge C_{t+dt} intersecting C_t (Figures 1b–1f). If none of the eddies at $t+dt$ intersects C_t, this eddy is considered to have disappeared (Figure 1b). If only one contour C_{t+dt} intersects C_t, the associated vortex is considered to be the same eddy that is tracked from t to $t+dt$. The temporal evolution of the eddy shape between t and $t+dt$ can exhibit two main patterns: (i) a simple translation characterized by contour intersections (Figure 1d) or not (Figure 1b); (ii) a size decay (Figure 1e) or growth (Figure 1f) without clear translation. If several contours C_{t+dt} intersect C_t (Figure 1c), a cost function (*CF*) is computed as:

$$CF=\sqrt{\left(\frac{\Delta R-\overline{\Delta R}}{\sigma_{\Delta R}}\right)^2+\left(\frac{\Delta A-\overline{\Delta A}}{\sigma_{\Delta A}}\right)^2+\left(\frac{\Delta EKE-\overline{\Delta EKE}}{\sigma_{\Delta EKE}}\right)^2} \quad (1)$$

where ΔR, ΔA, ΔEKE are, respectively, the radius, amplitude and eddy kinetic energy (EKE) variations between the vortex delimited by C_t and those intersecting C_t at time $t+dt$. $\overline{\Delta R}$, $\overline{\Delta A}$, $\overline{\Delta EKE}$ are determined for each EBUS by estimating average departures for a limited number (∼1000) of successfully formed tracks obtained from single contour intersections. Similarly $\sigma_{\Delta R}, \sigma_{\Delta A}, \sigma_{\Delta EKE}$ correspond to the standard deviation of the departures computed from the same set of ∼1000 trajectories. In contrast to the cost function used in [*Penven et al*., 2005] or *Chaigneau et al*. [2008, 2009], the standardization used in equation (1) means that each term on the right hand-side exhibit similar ranges and hence similar weights in the *CF*. Among all of

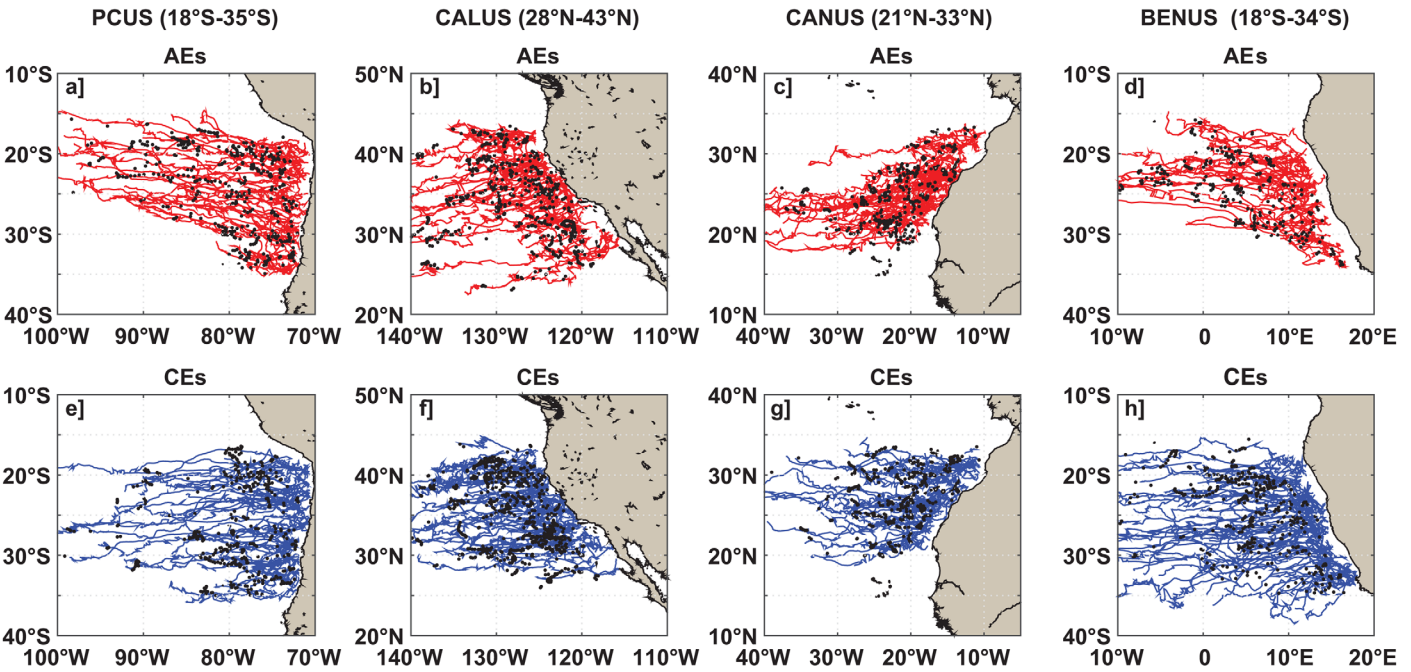

Figure 2. Trajectories of the (a–d) long-lived anticyclonic (in red) and (e–h) cyclonic eddies (in blue), formed between the coast and 400 km offshore in the four major Eastern Boundary Upwelling Systems. Only eddies having a lifetime longer than 30 days and sampled at least once by Argo floats (black dots) are shown. The meridional extent considered for each EBUS is also indicated in brackets.

the eddies intersecting C_t, the tracking algorithm selects the vortex that minimizes the *CF* and continues the eddy tracking until its disappearance.

Furthermore, eddy-merging or separation events frequently occur in the ocean. In case of an eddy-merging event, our algorithm considers that the trajectory after merging is the continuity of the oldest eddy, whereas the younger eddy trajectory is stopped. In contrast, if an eddy splitting event occurs, the cost function allows us to follow the more similar eddy along the trajectory while the less similar is considered as a new trajectory. In this study, we only retain "long-lived eddies" lasting more than 30 days and formed closer than ~400 km to the coast in the active upwelling centers of each EBUS (Figure 2), between January 2000 and December 2010. In agreement with previous studies [e.g., *Chaigneau et al.*, 2009], these main hot-spot regions of eddy generation extend from 18°S to 35°S in the PCUS [see *Fréon et al.*, 2009, Figure 1], from 28°N to 43°N in the CALUS [*Checkley and Barth*, 2009], from 21°N to 33°N for CANUS [*Arístegui et al.*, 2009] and from 18°S to 34°S for BENUS [*Fréon et al.*, 2009]. In each EBUS, between 400 and 500 "long-lived" AEs and CEs are generated in the upwelling areas (Table 1). These long-lived trajectories represent between 35% and 50% of the number of tracks formed near the coast, the rest are short-lived eddies. Note that it does not exist an official definition for "long-lived eddies" and, depending on the authors, the choice of their minimal duration can vary from a few weeks to several months [e.g., *Fang and Morrow*, 2003; *Chaigneau and Pizarro*, 2005; *Chaigneau et al.*, 2008; *Sangrà et al.*, 2009; *Kurczyn et al.*, 2012; *Chelton et al.*, 2007, 2011; *Chaigneau et al.*, 2009; *Chen et al.*, 2011]. Here we refer to "long-lived eddies" as eddies having a lifetime longer than 30 days, that is consistent with previous studies

Table 1. Number of Long-Lived Eddy Trajectories and Argo Float Profiles in the Four EBUS

	BENUS	CANUS	CALUS	PCUS
		Number of Long-Lived[a] *Trajectories*		
AEs	457	410	485	467
CEs	474	396	511	461
		Number of Trajectories Sampled by Argo Floats		
AEs	63	88	106	78
CEs	107	72	130	97
		Number of Argo Profiles		
OEs	2924	4527	8628	5147
AEs	1015	1369	2603	1710
CEs	879	1415	2529	1542
		Number of Argo Profiles Within Long-Lived Trajectories		
AEs	266	338	637	420
CEs	390	380	725	403

[a]Long-lived eddies correspond to eddies with a lifetime longer than 30 days.

and close to the typical e-folding timescale of ∼35 days used in the objective interpolation procedure for the SLA product [e.g., *Chelton et al*., 2011]. Increasing the minimal duration of the eddies does not strongly alter the results but obviously decreases the number of eddy trajectories and available in situ hydrographic profiles to depict their vertical structure.

2.2. Argo Float Profiles and Reconstruction of Thermohaline Vertical Structure of Mesoscale Eddies

Eddy vertical structures are investigated using autonomous Lagrangian profiling floats regularly released in the World Ocean as part of the international Argo program. Argo floats acquire temperature (T) and salinity (S) vertical profiles from ∼2000 m depth to the surface (further details on the Argo program can be found at http://www.ARGO.ucsd.edu/). Delayed-mode Argo data profiles from January 2000 to December 2010 were collected and made freely available by the Coriolis project (http://www.coriolis.eu.org). Only ascending records with a quality flag of 1 or 2 (corresponding to "good" and "probably good" quality data) are considered for the analysis. Similarly to *Chaigneau et al*. [2011], we only retained T/S profiles for which: (1) the shallowest data are above 15 m (corresponding to the shallowest mixed layer depth in the 4 EBUS) and the deepest data below 950 m depth, (2) the depth difference between two consecutive data does not exceed a given threshold (25 m for the 0–150 m layer, 50 m for the 150–300 m layer, 75 m for the 300–500 m layer and 100 m below 500 m depth), and (3) at least 30 T and S data are available between the surface and 950 m depth. In each EBUS, the Argo profiles passing these criteria represent 60–85% of the total set of available profiles. These retained profiles are then linearly interpolated every 10 m from the surface (assuming the shallowest data correspond to the surface) to the deepest available level, and potential temperature (θ) and dynamic height (DH) relative to 950 m are computed. Finally, θ/S profiles were visually checked and those presenting suspicious data were systematically discarded (∼1% of the profiles).

The vertical profiles are then classified into 3 categories depending on whether the Argo floats surfaced within the AEs or CEs detected from the altimetry maps and formed in the active upwelling regions, or outside these eddies (OEs). In average, ∼62% of the retained Argo profiles were "OEs," ∼20% within AEs and ∼18% within CEs (Table 1). Around ∼70% of the Argo profiles surfacing within eddies belong to trajectories generated outside of the active upwelling areas, or with lifetimes shorter than 30 days, and so are not analyzed in this study. Among the total number of retained long-lived trajectories, 20% were sampled by Argo floats at least once (Table 1). The least well sampled region was the Benguela upwelling system, and the California region had the best sampling.

In order to describe the θ and S perturbations associated with eddies, we computed θ and S anomalies (θ' and S′ respectively), by removing from each Argo profile a local mean climatological profile representative of the large-scale background temperature and salinity fields. As in *Castelao* [2014], these local mean profiles were obtained by averaging all the available θ and S Argo casts acquired within a radius of 200 km and separated by less than $\pm$ 30 days from the month date of the considered profile, but including profiles from any year. Similarly, a local mean dynamic height (DH) is computed and removed from the DH of the considered profile, to obtain a dynamic height anomaly (DH′) profile associated with the eddy.

2.3. Clustering Analysis

Although CEs and AEs can be described by their mean vertical structure [*Chaigneau et al*., 2011; *Kurian et al*., 2011; *Yang et al*., 2013; *Castelao*, 2014], different eddy types can coexist in each region (e.g., surface or subsurface-intensified, multicores eddies, etc) and thus influence the shape of the mean vertical structure. In order to determine the main eddy-types observed in each EBUS, we applied the following procedure. First, for each eddy trajectory sampled by Argo floats, we computed its averaged temperature and salinity anomaly profiles, regardless of the distance between the profiles and the eddy centers, assuming that each eddy conserves its general vertical shape during its lifetime. Second, a hierarchical ascending classification (HAC) technique, was applied to these trajectory-averaged profiles. Readers interested in more details on clustering techniques are referred to *Roux* [1985].

Briefly, the HAC considers each mean vertical profile as a singleton cluster (i.e., a class of one object) and then successively agglomerates pairs of clusters based on their similarities until all singleton clusters have been merged into a single cluster containing all the trajectory-averaged vertical profiles (i.e., one class containing all the objects). Thus, the HAC basically consists of a three-step procedure:

Table 2. Mean Long-Lived Eddy Characteristics in the Four EBUS[a]

	BENUS	CANUS	CALUS	PCUS
		Radius (km)		
AEs	93 ± 38 (141 ± 30)	91 ± 35 (135 ± 29)	83 ± 35 (118 ± 30)	93 ± 39 (131 ± 31)
CEs	100 ± 46 (153 ± 30)	95 ± 37 (137 ± 32)	83 ± 38 (123 ± 33)	98 ± 41 (140 ± 33)
		Amplitude (cm)		
AEs	4.6 ± 4.7 (9.2 ± 5.2)	3.9 ± 3.1 (8.1 ± 4.1)	5.9 ± 4.5 (10.6 ± 5.6)	4.2 ± 2.7 (6.9 ± 2.7)
CEs	7.6 ± 10.3 (15.6 ± 10.4)	3.9 ± 2.8 (7.3 ± 3.3)	6.8 ± 5.2 (12.1 ± 5.0)	5.4 ± 3.6 (9.1 ± 2.9)
		Lifetime (months)		
AEs	4.5 ± 5.6 (12.3 ± 8.0)	5.5 ± 6.7 (14.6 ± 8.5)	6.2 ± 7.7 (15.4 ± 11.1)	6.4 ± 7.5 (15.7 ± 9.8)
CEs	6.1 ± 7.0 (15.0 ± 7.6)	5.2 ± 6.3 (14.1 ± 8.8)	6.3 ± 7.5 (14.6 ± 10.0)	6.9 ± 7.5 (15.3 ± 8.7)
		Total Distance of Propagation (km)		
AEs	230 ± 330 (799 ± 419)	416 ± 574 (1198 ± 772)	271 ± 380 (706 ± 597)	457 ± 626 (1253 ± 885)
CEs	429 ± 469 (1059 ± 390)	386 ± 544 (1139 ± 713)	280 ± 398 (715 ± 534)	507 ± 626 (1163 ± 766)

[a]Numbers indicate the average ±1 standard deviation. Values without parentheses correspond to all the long-lived eddies whereas values within parentheses correspond to long-lived eddies sampled by Argo floats.

1. Measure the similarity or dissimilarity (usually called distance) between every pair of objects (in our case, the trajectory-averaged profiles). At each depth, we normalized the θ/S anomalies of all the averaged profiles, and compute Euclidean distances between every pair of data. Note that due to the normalization, the results are more impacted by the general vertical shape of the profiles rather than the intensity of the anomalies.
2. Apply an agglomerative clustering algorithm that links the objects that are mathematically the most similar and regroup them into a binary cluster tree, called dendrogram. Here this is achieved using the Ward's aggregation method that minimizes the intra-cluster variance and maximizes the total inter-cluster variance [*Roux*, 1985; *Ward et al*., 1963].
3. Determine where to cut the cluster tree to retain the most significant clusters and adequately partition the data. In order to determine the optimal number of clusters that correspond to the main eddy-types observed in each EBUS, we used the dendrogram which is representative of the strength of the dissimilarities between groups. Each cluster retained in the dendrogram represents a specific type of eddy, associated with a particular vertical structure.

The main components impacting on the cluster partition are the θ' and S′ anomalies. Considering DH′ within the cluster analysis does not improve the partition of the data and this parameter was not retained as an input parameter in the HAC. However, once the profiles are separated in distinct homogeneous groups (e.g., clusters) using the θ' and S′ in the HAC, the DH′ corresponding to these profiles can be further investigated.

Finally, in order to estimate the statistical significance of each retained cluster, their mean temperature, salinity and dynamic height anomaly profiles were compared with random samplings of profiles located outside of the eddies. We adopted a Monte Carlo approach using bootstrap tests of significance. For a cluster composed by *N* trajectories, we randomly selected *N* temperature, salinity and dynamic height anomaly profiles OEs and averaged them. We repeated this procedure to obtain 10 000 replicates for which the results converged. The 95% confidence interval was obtained from these 10 000 replicates. A cluster is considered significant if most of its mean vertical temperature and salinity values fall outside of this 95% confidence interval.

3. Results

3.1. Mean Surface Characteristics of Mesoscale Eddies in the EBUS

As previously observed, large mesoscale eddies are formed near the coast in eastern boundary regions and propagate offshore over long distances, with a general tendency for long-lived AEs (CEs, respectively) to be slightly deflected equatorward (poleward) (Figure 2) [*Cushman-Roisin et al*., 1990; *Morrow et al*., 2004; *Chaigneau et al*., 2009; *Chelton et al*., 2011]. The averaged equatorward deflection for AEs varies from +8° from the westward direction in the BENUS to more than +20° in the CALUS. In contrast the averaged poleward deflection for CEs varies from −3° to −10° from the westward direction in all the EBUS, except in the CALUS where the CEs are also slightly deflected equatorward with a mean angle of +6°.

On average, long-lived eddies generated in the four EBUS have typical radii of 80–100 km, amplitudes of 4–8 cm, lifetimes of 5–7 months and move westward over 250–500 km (Table 2). Values of the eddy radii

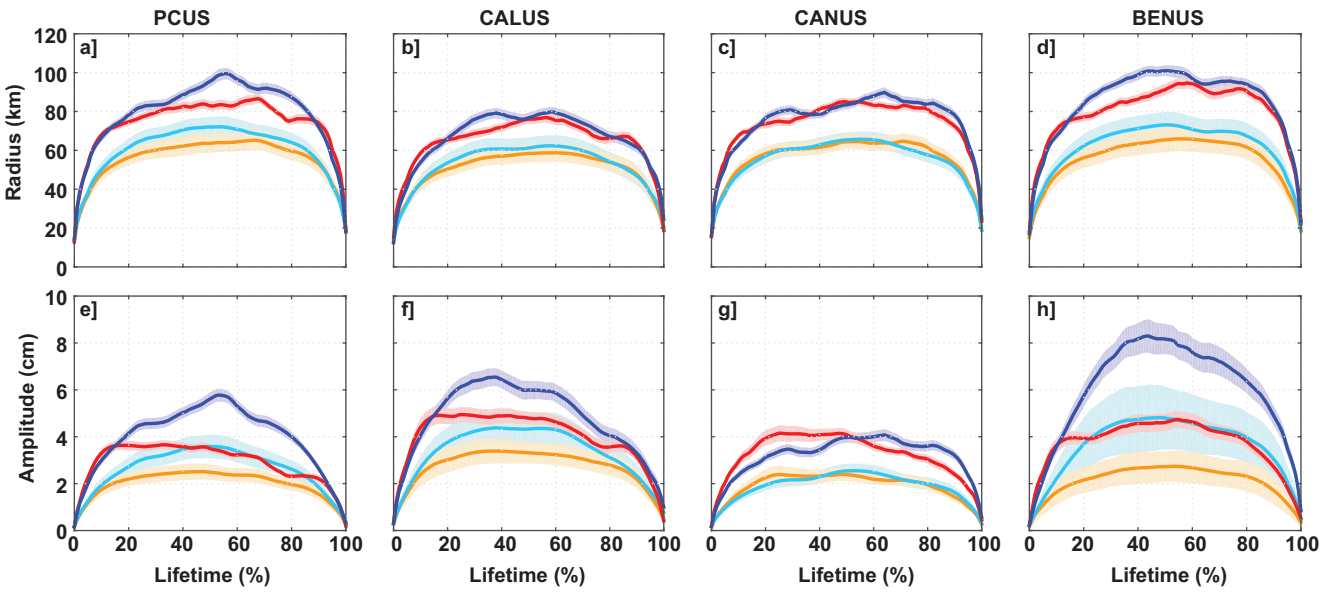

Figure 3. Ensemble mean (solid lines) and error (shading areas) of (a–d) radius and (e–h) amplitude as a function of dimensionless time for the altimeter-tracked long-lived eddies. Orange (cyan, respectively) lines correspond to all the identified AEs (CEs), whereas red (blue) lines correspond to AEs (CEs) sampled at least once by Argo floats. Errors of the mean were evaluated using Student's *t* test with a significance level of 95%.

are mainly controlled by the latitudinal extent of each EBUS (e.g., smaller radii at higher latitudes as for the CALUS). Eddies of the CANUS and PCUS exhibit slightly smaller amplitudes than in the BENUS and CALUS. Eddies in the CALUS have the weakest propagation velocities [*Chaigneau et al*., 2009] and travel over shorter distances, but they still have comparable lifetimes. There is no significant difference between the CEs and AEs in the EBUS, except for the BENUS where AEs have on average smaller radius, amplitude, lifetime and travel less than the CEs (Table 2). It should be noted that some eddies leave the studied areas before dissipating and should be associated with longer lifetimes, but it only concerns a few trajectories (Figure 2) and the statistics presented in Table 2 should not be strongly biased. Interestingly, the 20% of long-lived eddies sampled by Argo floats are much larger (120–150 km), have higher amplitudes (7–16 cm), longer lifetimes (12–16 months) and travel farther from the coast (700–1300 km), regardless of polarity. This indicates that Argo floats preferentially surface in larger, more intense and longer lived eddies.

It has been recently recognized that during their lifetime, eddies typically exhibit a three-step evolution composed of growth, mature and decay phases, regardless of their lifetime duration. This has been observed both regionally using model simulations [*Kurian et al*., 2011] and altimetry data [*Chaigneau et al*., 2008; *Liu et al*., 2012] and globally [*Samelson et al*., 2014]. In the 4 EBUS, the mean evolution of the eddy radius and amplitude along their normalized life-cycle also shows these 3 distinct phases (Figure 3). As expected from Table 2, the set of eddy trajectories sampled by Argo floats exhibits higher mean values than the total set of trajectories generated near the coast. However, the temporal evolution of their eddy radius and amplitude show more fluctuations due to the more limited number of sampled trajectories (Figure 3). Except for the CANUS, the CEs of all the EBUS exhibit significant higher radii and amplitudes during their mature phase than the AEs, and the BENUS CEs are particularly strong. The higher amplitude for the BENUS CEs are likely due to the subsurface-intensified CEs that are much stronger than the subsurface AEs in this EBUS (see sections 3.2.4 and 4.1).

Normalizing the evolution of the radius and amplitude by their respective maxima, we can compute a growth speed expressed per time unit (Figure 4). Following *Samelson et al*. [2014], this speed is computed between 0 and 15% of the lifetime for the growing phase, between 15 and 85% for the mature phase and between 85 and 100% for the decay phase. Averaged over the four EBUS, the growth rate for amplitude and radius do not depend on the eddy polarity or size. The absolute values obtained for the growing and the decay phase are very similar. This result is in agreement with *Samelson et al*. [2014], who found that the evolution of the amplitude during the eddy lifetime was symmetric over time, despite the difference on the number of eddies used in the studies ($\sim 2.10^5$ in *Samelson et al*. [2014] compared to $\sim$450 in the present study).

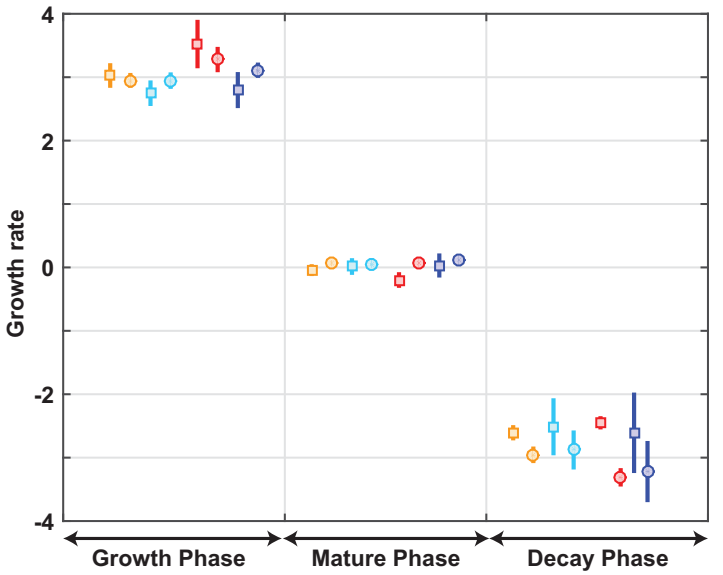

Figure 4. Averages of the normalized radius (circles) and amplitude (squares) growth rates per percentage of the lifetime during the growth, mature and decay phases in the four EBUS. Error bars correspond to the standard deviation between the four EBUS. Orange (cyan, respectively) symbols correspond to all the identified long-lived AEs (CEs), whereas red (blue) symbols correspond to AEs (CEs) sampled at least once by Argo floats.

In addition to the surface characteristics of these eddies, we are able to provide a three-dimensional description of their evolution using Argo floats colocalized within them. The next section depicts the different eddy-types we found in each system and their mean thermohaline structure observed during their lifetimes.

3.2. Main Eddy-Types and Associated Vertical Structures in the EBUS

3.2.1. Peru-Chile Upwelling System (PCUS)

The HAC analysis (or clustering) and associated dendrogram (not shown) suggest that the AEs of the PCUS can be separated into two main eddy-types (Figure 5). The first cluster represents 55% of the sampled trajectories (Figure 5a). This cluster corresponds to subsurface-intensified AEs characterized by relatively strong positive θ' and S′ between 200 m and 600 m depth (Figures 5b and 5c). The mean DH′ associated with this cluster also shows significant positive anomalies above 600–800 m depth (Figure 5d). These subsurface-intensified eddies are formed all along the coast (Figure 5a), mainly shed by the near-coastal poleward Peru-Chile Undercurrent [*Johnson and McTaggart*, 2010; *Chaigneau et al*., 2011; *Colas et al*., 2012; *Hormazabal et al*., 2013], that flows along the continental slope between ∼100 and 500 m depth [*Silva and Neshyba*, 1979; *Chaigneau et al*., 2013]. This eddy-type carries relatively warm (∼12.5°C) and salty (34.9) water of equatorial origin [*Silva et al*., 2009] and induces typical θ' and S′ of 0.5°C and 0.05, respectively (Figures 5b and 5c). These subsurface eddies are generally associated with a doming of the upper pycnocline leading to the weak negative θ' and S′ observed between the surface and 100 m depth, and a deepening of the lower pycnocline enhancing the positive subsurface anomalies [*Chaigneau et al*., 2011; *Colas et al*., 2012]. The DH′ is also slightly reduced in the surface layer (Figure 5d).

The mean θ' and S′ of the second cluster (45% of the trajectories) are associated with surface-intensified AEs with maximum anomalies above the seasonal pycnocline (Figures 5f and 5g). However, although these mean θ' and S′ are very weak and not statistically significant, these eddies are on average associated with a weakly significant positive DH′ in the surface layer (Figure 5h). These weak AEs are generated all along the coast (Figure 5e) and exhibit smaller radii but similar amplitudes compared with the subsurface AEs (not shown). The temporal evolution of their vertical structure along the eddy lifetime confirms that surface eddies are not robust (not shown), as their θ' and S′ show rapid but weak changes from one profile to another. Such behavior suggests that these surface-intensified AEs are mainly influenced by the ocean-atmosphere interactions that continuously modify the water mass properties transported in the surface layers. In contrast, the composite of the subsurface-intensified anticyclonic eddy-type profiles shows more homogeneous θ', S′ and DH′ along their lifetime (Figures 7a–7c). Thus even if the surface layers are impacted by air-sea exchanges, these eddies are well isolated and carry the relatively warm and salty water of the Peru-Chile Undercurrent into their cores over long distances and without strong modifications. Nevertheless, the temporal evolution of the vertical structure for this subsurface-intensified eddy-type (Figures 7a–7c) does not exhibit strong variations during the three phases as was observed in the amplitude and radius evolutions (Figure 3). Moreover, despite the consequent number of Argo profiles entering the

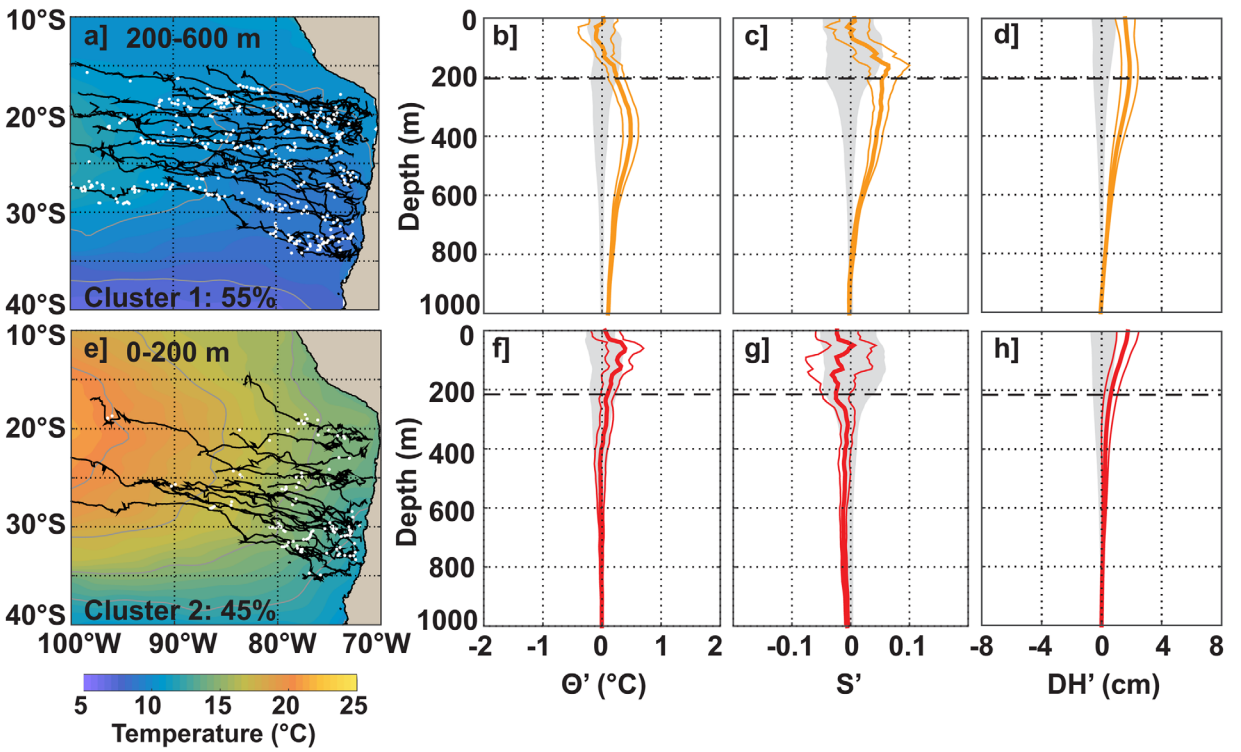

Figure 5. Clustering analysis of the Argo profiles surfacing within the long-lived anticyclonic eddies formed in the PCUS. (a, e) For each cluster, the associated trajectories (black lines) and Argo float positions (white dots) are superimposed on the climatological temperature field, averaged within the indicated layers. (b, f) Mean temperature, (c, g) salinity, and (d, h) dynamic height anomaly profiles, averaged for each trajectory of the associated cluster, correspond to the thick lines, whereas errors evaluated using Student's *t* test with a significance level of 95% around the mean are indicated by thin lines. Gray shading represent random errors estimated from Argo float profiles surfacing outside eddies (see text for details). Horizontal dashed thick lines correspond to the depth of the base of the pycnocline estimated from Argo floats surfacing within eddies.

vertical structure evolution, we are still facing a lack of sampling especially during the growth (11% of the available profiles) and the decay phases (8% of the available profiles).

The cluster analysis applied to the CEs also reveals the presence of two main CE-types in the PCUS (Figure 6). Eddies associated with the first cluster, that represents 88% of the trajectories, are formed all along the coast (Figure 6a) and show maximum negative θ', S′ and DH′ in the near-surface layers above the seasonal pycnocline (Figures 6b–6d). These surface-intensified eddies, with maximum mean anomalies of −0.4°C in temperature and −0.04 in salinity, have been previously documented and are likely shed by the near-coastal equatorward surface currents [*Chaigneau et al.*, 2011; *Colas et al.*, 2012]. They have however a weak signature at depth extending down to ∼500 m depth with significant θ' and DH′ (Figures 6b and 6d). These weak anomalies are probably not transported by the eddy cores but more likely due to the local eddy-induced upwelling associated with the surface-intensified CEs [*Chaigneau et al.*, 2011]. The composite temporal evolution of S′ associated with this eddy type as a function of lifetime shows a saltier S′ between 100 and 200 m depth beneath a fresher surface S′ (Figure 7e). As the composite eddy evolves and propagates westward, both the positive and negative S′ deepen, leading to an almost null average between 100 and 300 m depth (Figure 6c). Most of the profiles constituting this surface-intensified cluster are located in a region of relatively fresh Eastern South Pacific Intermediate Water (ESPIW) between 150 and 250 m depth [*Schneider et al.*, 2003]. This water mass is commonly observed south of 20°S [*Schneider et al.*, 2003] but can have a signature as North as ∼14°S [*Pietri et al.*, 2013, 2014]. The positive S′ observed in Figure 7e can be due to both the advection of saltier coastal water by the cyclones into the fresher ESPIW and the CE-induced upwelling of deeper and saltier water into this water mass (Figures 6a and 6e).

The second cluster obtained for the CEs is composed of only 12% of the trajectories sampled by Argo floats. However, this cluster is significant with strong negative θ' and S′ that are maximum near ∼500 m and extend down to ∼800 m depth (Figures 6f and 6g). The mean DH′ is also significant above 800 m and shows a maximum negative anomaly of −3.5 cm above the pycnocline (Figure 6h). To the best of our

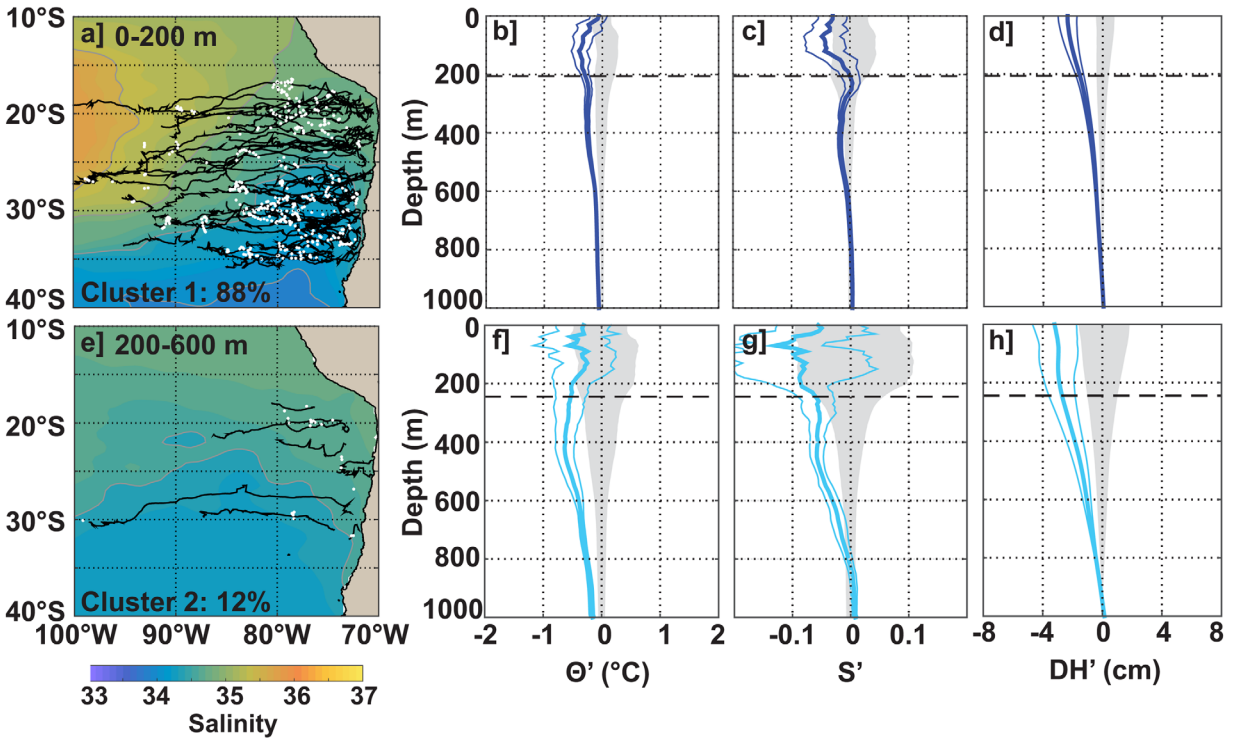

Figure 6. Same as Figure 5 but for the long-lived cyclonic eddies formed in the PCUS. Note that color shading in Figures 6a and 6e now corresponds to the climatological salinity field, averaged within the indicated layers.

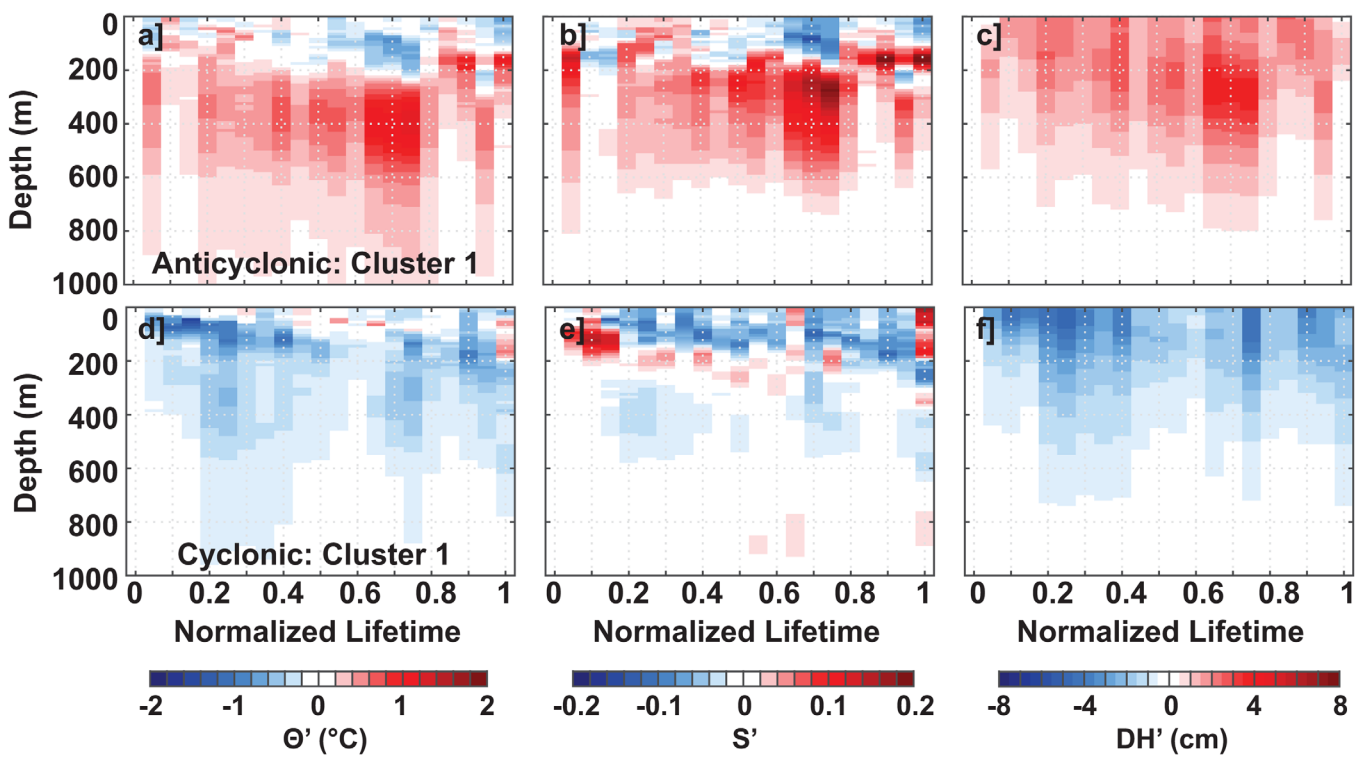

Figure 7. Temporal evolution of the mean (a, d) temperature, (b, e) salinity, and (c, f) dynamic height anomalies as a function of the normalized lifetime (dimensionless time) for the a-c] subsurface-intensified AEs and the (d, f) surface-intensified CEs of the PCUS, obtained from the Argo float profiles shown in Figures 5a and 6a, respectively. All the anomaly profiles were positioned at the time they were acquired relative to the corresponding eddy lifetimes and were further averaged every 5% of the normalized lifetime.

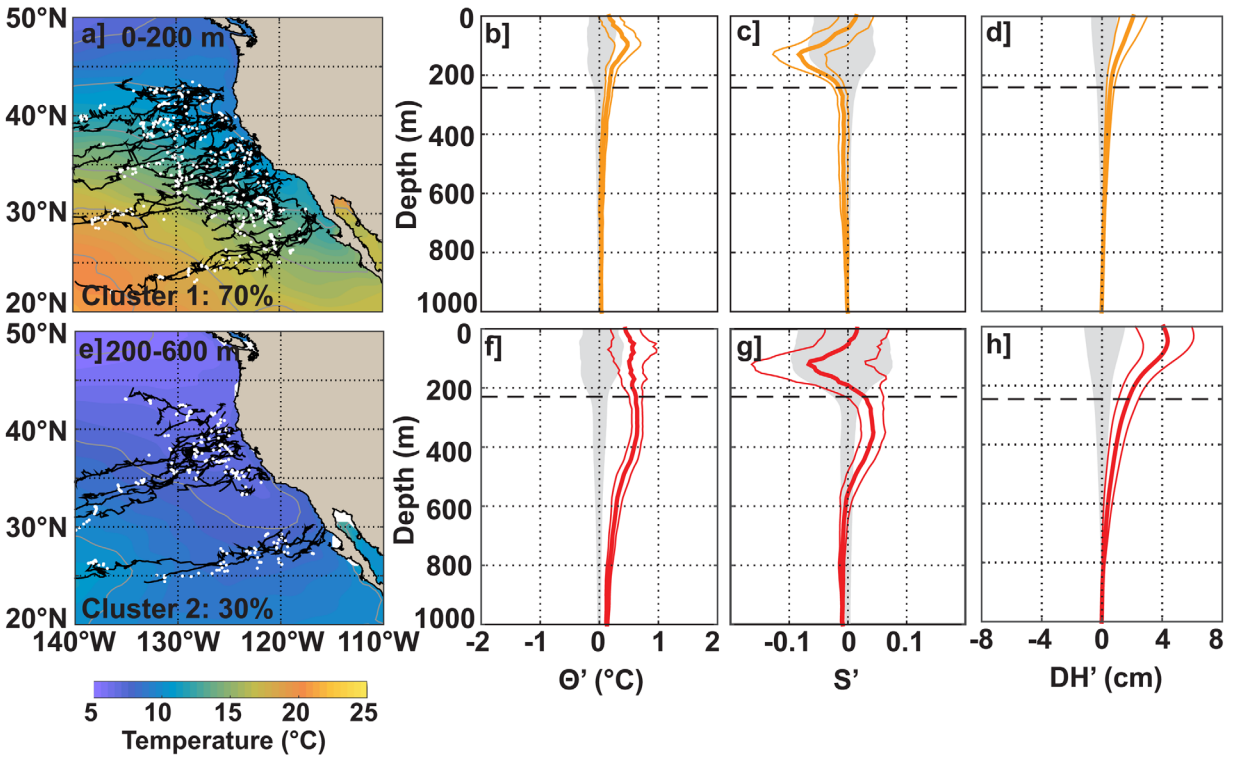

Figure 8. Same as Figure 5, but for the CALUS anticyclones.

knowledge, only one subsurface-intensified CE vertical structure has been previously documented in the PCUS [*Chaigneau and Pizarro*, 2005]. As for the subsurface AEs, these rarely observed subsurface-intensified CEs tend to have slightly larger radii and higher amplitudes than the surface-intensified eddies (not shown). Unfortunately, the limited number of Argo profiles in this cluster (Figure 6e) prevent us to study the temporal evolution of the vertical structure.

3.2.2. California Upwelling System (CALUS)

In the CALUS, the cluster analysis also suggests the presence of two main AE types (Figure 8). The first cluster regroups 70% of the sampled trajectories and shows maximum warm θ' (0.4°C) and fresher S′ (−0.08) near 150 m depth (Figures 8b and 8c). Significant anomalies are restricted to depths above the pycnocline and the majority of the sampled AEs are thus surface-intensified, as also suggested by the averaged DH′ profile (Figure 8d). These eddies are formed all along the California coast (Figure 8a) with some preferential generating areas, near Point Arena (39°N), Point Reyes (38°N), Point Conception (35°N) and Point Eugenia (28°N). These sites have been previously recognized as hot spots for eddy generation [*Chaigneau et al*., 2009; *Kurian et al*., 2011]. The observed negative S′ (Figure 8c) is probably due to the local eddy-induced downwelling of the surface layers composed of fresh Pacific Subarctic Water [*Simpson et al*., 1984; *Emery and Meincke*, 1986; *Huyer et al*., 1991; *Checkley and Barth*, 2009; *Dong et al*., 2012] that can be clearly identified in Figure 9a (color shading). The temporal evolution of the corresponding composite anomalies is consistent with their mean profiles and their intensity does not present strong variations between the growth, mature and decay phases (Figures 10a–10c). However, a progressive deepening of the θ/S anomalies is observed (Figures 10a and 10b) and is associated with the large-scale deepening of the thermocline, halocline and pycnocline from near-coastal regions to the open ocean. This deepening does not strongly impact the shape of the DH′ profiles (Figure 10c).

The second cluster of AEs, that represents 30% of the trajectories, shows significant and intense warm θ' and salty S′ between 200 and 550 m depth, with maximum values of 0.8°C and 0.06 respectively (Figures 8f and 8g). This AE type corresponds to the subsurface-intensified eddies shed by the California Undercurrent known as "Cuddies" [*Simpson et al*., 1984; *Simpson and Lynn*, 1990; *Huyer et al*., 1998; *Garfield et al*., 1999; *Jerónimo and Gómez-Valdés*, 2007; *Kurian et al*., 2011; *Collins et al*., 2013; *Pelland et al*., 2013]. In contrast to those observed by *Simpson et al*. [1984, 1990] and *Collins et al*. [2013], the Cuddies presented here do not

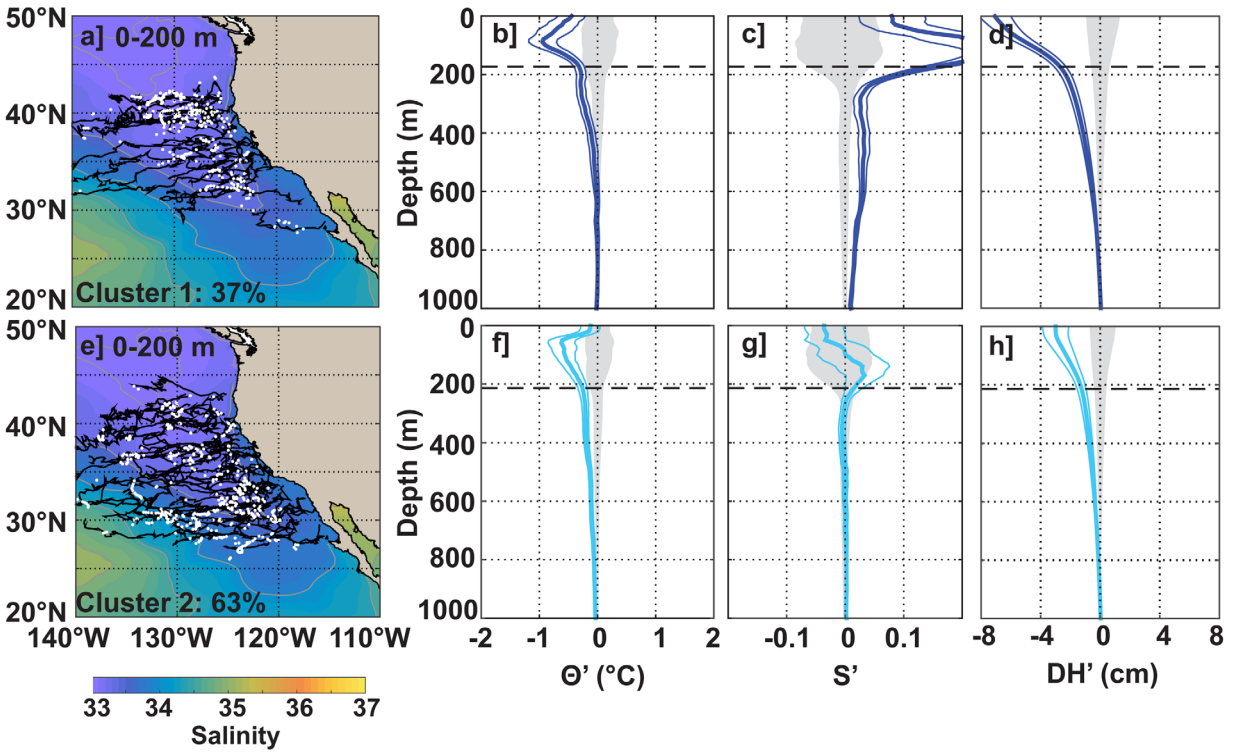

Figure 9. Same as Figure 6, but for the CALUS cyclones.

show negative θ' in the upper 100 m in response to the doming of the isopycnals. Again, these subsurface-intensified eddies are mainly generated at some hot-spots (Figure 8e), near Cape Blanco (42°N), Cape Mendocino (40°N) and Point Arena (39°N) in the Northern part, and near Point Conception (35°N) and Punta Eugenia (28°N) in the Southern part. These regions are known to generate eddies by mean flow destabilization [*Batteen et al*., 2003; *Jerónimo and Gómez-Valdés*, 2007; *Pelland et al*., 2013].

The temporal evolution of the vertical structure of the Cuddies shows a significant intensification in both θ' and S′ around 40% of their lifetime (Figures 10d and 10e), different from the typical transition phases observed from surface characteristics (e.g., Figure 3), whereas the temporal evolution of the DH′ remains almost constant along the lifetime (Figure 10f). These eddies are propagating toward the subtropical gyre (Figure 8e), composed of warmer and saltier water, which should reduce their initial anomalies of temperature and salinity. The intensification of θ' and S′ in the subsurface is more likely due to an increase number of Argo floats within particularly strong eddies between 40% and 80% of their lifetime. Effectively, ∼20% of the profiles of this cluster belong to 3 intense eddies generated near Punta Eugenia and sampled after 40% of their lifetime. Although the observed intensification could also be due to a closer position of the Argo profiles relative to the eddy center where the anomalies are expected to be maximum, we did not observed a clear modification of this distance. Even though the number of eddies sampled by Argo floats is limited, the ratio of the surface and subsurface-intensified AEs of 7:3 is similar to the ratio of 3:2 found by *Kurian et al*. [2011] in a model simulation. In this EBUS, no significant difference was observed between the characteristics (radius and amplitude) of the surface and subsurface-intensified AE types.

The clustering analysis applied to the CEs of the CALUS also suggests two main CE-types (Figure 9). Both of these eddy-types correspond to surface-intensified eddies, with maximum θ', S′ and DH′ above the seasonal pycnocline (Figures 9b–9d and 9f–9h). The two clusters also exhibit similar mean radii and amplitudes (not shown). The anomalies associated with the first cluster, representing 37% of the CE trajectories, are much more intense, with maximum θ' of −1°C and S′ of 0.23 at ∼100 m depth (Figures 9b and 9c), and maximum DH′ of −6.5 cm at the sea-surface (Figure 9d). The signature of this eddy-type extends down to ∼400 m in temperature, and ∼700–800 m in salinity and dynamic height. These eddies are almost exclusively formed north of 35°N (Figure 9a) and cross the fresh tongue of the Pacific Surface Water carried in the surface layers

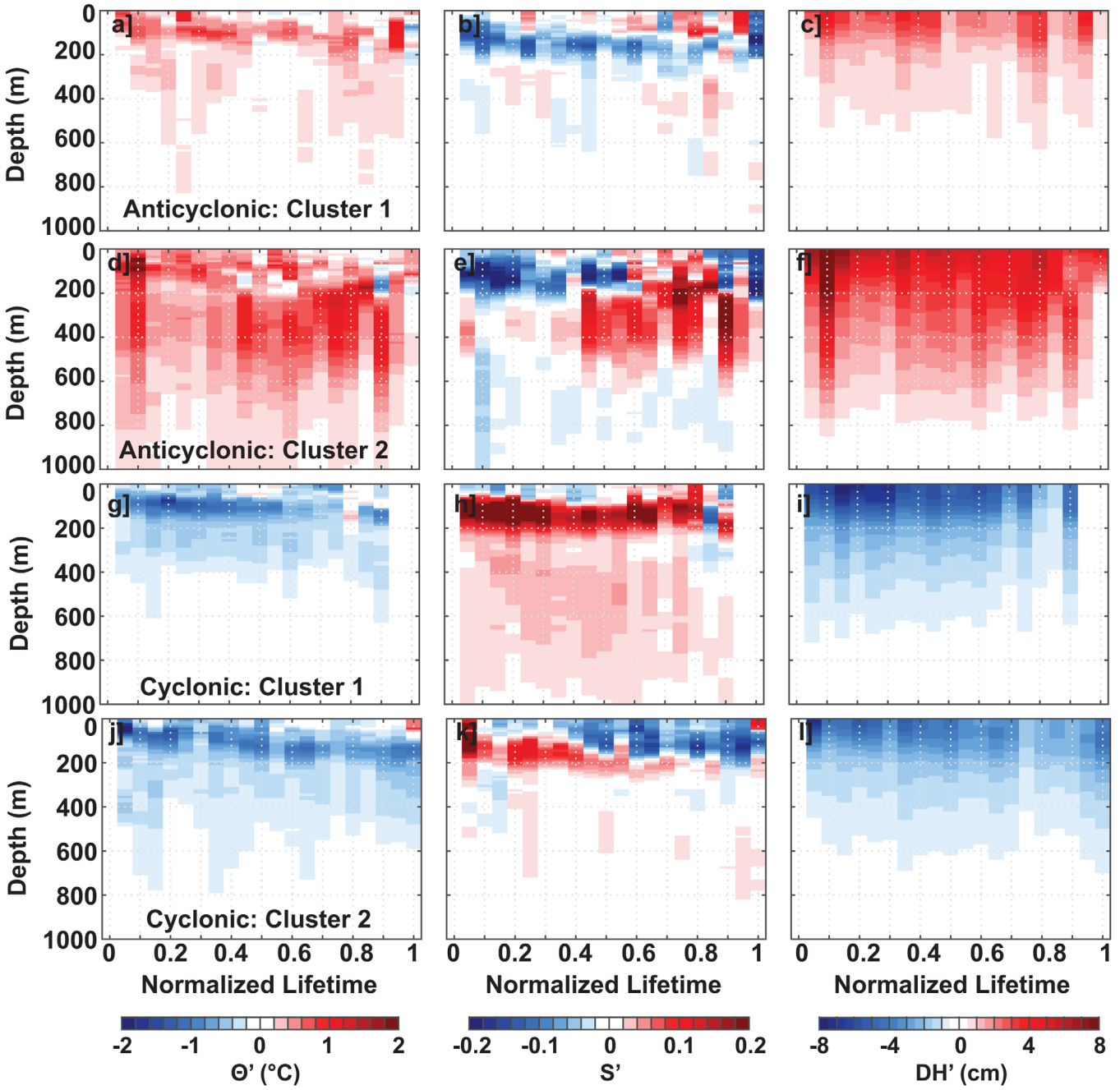

Figure 10. Same as Figure 7, but for the CALUS. (a–f) AE clusters shown in Figure 8. (g–l) CE clusters shown in Figure 9.

by the California Current [*Simpson et al.*, 1984; *Emery and Meincke*, 1986; *Huyer et al.*, 1991; *Checkley and Barth*, 2009; *Dong et al.*, 2012]. Both the shoaling of the isopycnals associated with these surface-intensified eddies and the advection of saltier near-coastal water across fresher offshore waters can lead to this observed positive S′. The temporal evolution of the vertical structure of this eddy-type is homogeneous during the growth and mature phases (Figures 10g–10i) in contrast to what is observed for the altimeter-derived radius and amplitude. However, only 2 Argo profiles are available during the decay phase that prevent us to describe this phase.

The second cyclonic eddy-type presents similar vertical characteristics (Figures 9f–9h) but the θ', S′ and DH′ are weaker. Temperature and dynamic height anomalies suggest a vertical extend down to 600 m depth, but salinity anomalies are almost null below the seasonal pycnocline. This eddy-type represents more than

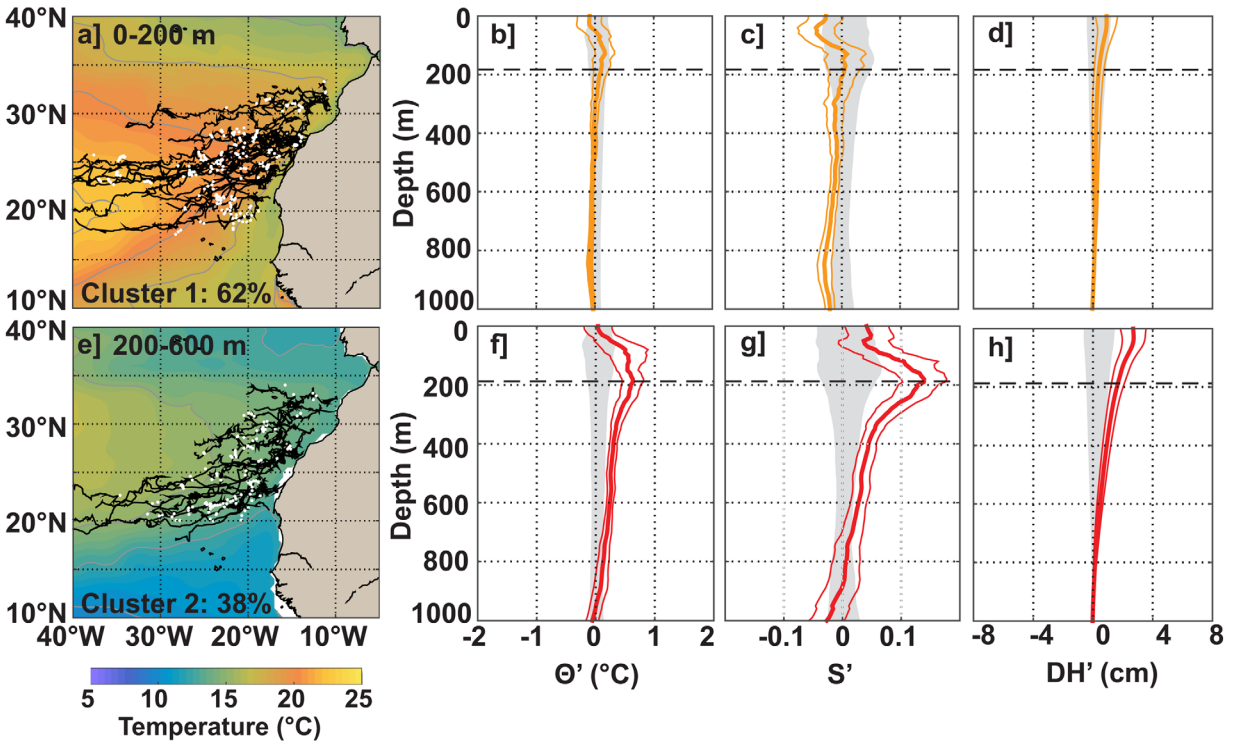

Figure 11. Same as Figure 5, but for the CANUS anticyclones.

60% of the sampled CEs, and is formed all along the California coast (Figure 9e), with the major part of the Argo profiles located south of 35°N where the salinity minimum associated with the Pacific Surface Water is less pronounced. The offshore evolution shown in Figure 10k presents a progressive deepening of the positive S′ located below a negative S′, in a similar way to the surface-intensified CEs of the PCUS (Figure 7e). This leads to a compensation between the positive S′ at the beginning of the lifetime, as the eddies cross relatively fresher water, and the negative S′ later, when the eddies are evolving in the saltier water of the subtropical gyre (Figure 9g and Figure 10k).

3.2.3. Canary Upwelling System (CANUS)

In the CANUS, the clustering analysis also suggests the presence of two main AE and CE types. The first cluster of AEs, regrouping more than 60% of the trajectories, is associated with weak eddies that on average exhibit nonsignificant θ', S′ and DH′ (Figures 11b–11d). These trajectories are generated all along the coast of the CANUS (Figure 11a), but more particularly between 25°N and the Canary Islands. This region presents an enhanced eddy generation due to the unstable currents and winds [*Arístegui et al*., 1994, 1997; *Barton et al*., 1998; *Pacheco and Hernandez-Guerra*, 1999; *Barton and Arístegui*, 2004; *Sangrà et al*., 2009]. In contrast, ∼40% of the sampled trajectories are associated with subsurface-intensified eddies showing significant maximum θ' of 0.6°C and S′ of 0.12 around the pycnocline depth and extending down to ∼500 m depth (Figures 11f and 11g). The DH′, which is also significantly positive above 500 m depth, reaches a maximum value of 3 cm at the sea-surface (Figure 11h). The observed vertical structure of this eddy-type is similar to the Shallow Subtropical Subduction Westward-propagating Eddies (Swesties) described by *Pingree* [1996]. These Swesties also exhibit a relatively warm and salty core of 150 m thick and centered at 190 m depth. Our vertical structure is also comparable to the results presented by *Arístegui et al*. [1994]. This eddy-type is more particularly generated in three subregions (Figure 11e): between Cape Beddouza (32°N) and Cape Ghir (30.5°N), presented as the "Madeira Corridor" by *Sangrà et al*. [2009]; near the coast just south of the Canary Islands between 25°N and 28°N, corresponding to the northern part of the "Canary Corridor" [*Sangrà et al*., 2009]; and between 23°N and 24.5°N, corresponding to the southern part of the "Canary Corridor." As they are drifting west south-westward along the Canary Current path, they traverse a relatively stable background field, with only a slight warming and salinity increase to the west (see shading colors in Figures 11a and 11e, and 12a and 12e). Indeed, their vertical structure evolution remains almost stable with no observed influence due

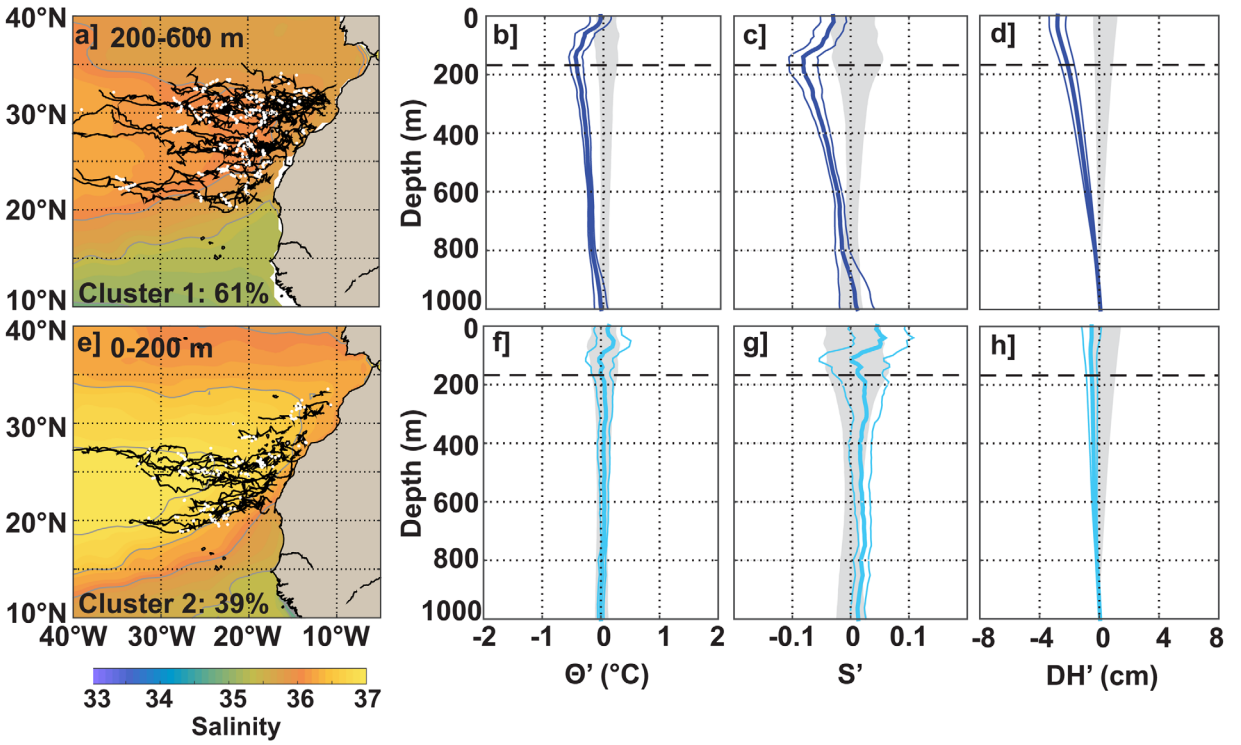

Figure 12. Same as Figure 6, but for the CANUS cyclones.

to the change in the background fields nor a decrease in their anomalies during their dissipation phase (Figures 13a–13c). This second cluster is associated with eddies having larger radii, higher amplitudes and longer lifetimes than the first cluster (not shown), but they are formed essentially in the same regions.

The CEs of the CANUS can also be separated in two main groups. The first cluster, representing ∼60% of the trajectories, shows maximum negative θ' and S′ of −0.5°C and −0.07 near 200 m depth, at the level of the seasonal pycnocline (Figures 12b and 12c). The core of these subsurface-intensified eddies extends on average down to 600–800 m depth with significant negative anomalies that have a clear signature on the DH′ profile which is maximum at the surface (Figure 12d). Compared to the other eddy-types in this EBUS, these subsurface-intensified eddies are more particularly generated in the "Madeira Corridor" described by *Sangrà et al.* [2009], north of the Canary Islands (Figure 12a). The second cluster, that regroups ∼40% of the sampled trajectories, shows on average weak and nonsignificant anomalies (Figures 12f–12h). In contrast to the first cluster, most of these weak eddies are formed in the Southern part of the CANUS and propagate south-westward (Figure 12e). These eddies are characterized by smaller amplitudes and shorter lifetimes than the first cluster (not shown).

There is little temporal evolution in the vertical structure of the subsurface CEs after their formation (Figures 13d–13f), and θ' S′ and DH′ evolution remain close to the mean vertical structure of the clusters shown in the Figures 12b–12d. For the CEs, the initially cold and fresh upwelled water near the coast combined with the local eddy-induced upwelling within the cyclones generates negative θ' and S′ which are conserved along the eddy lifetime. The background temperature and salinity climatological maps (Figures 11a, 11e, 12a, and 12e) show that these CEs trajectories are crossing isotherms between 200 and 600 m depth, but there are fewer Argo profiles in the saltiest and warmest part of the gyre, at the end of the eddy lifetimes. We were expecting some intensification in the anomaly evolution, as some very long CEs, with lifetimes longer than 450 days, traveled across warmer and saltier waters in the western part of the region. These few very long-lived eddies were well sampled during their mature phase and represent more than half of the profiles available between 50% and 85% of the normalized lifetime. Thus, the slight increase of θ', S′ and DH′ observed between 50% and 70% of the mean normalized lifetime may be related to these particularly long-lived eddies (Figures 13d–13f). In contrast, the Argo profiles that sampled these eddies only represent a quarter of the available profiles in the decay phase.

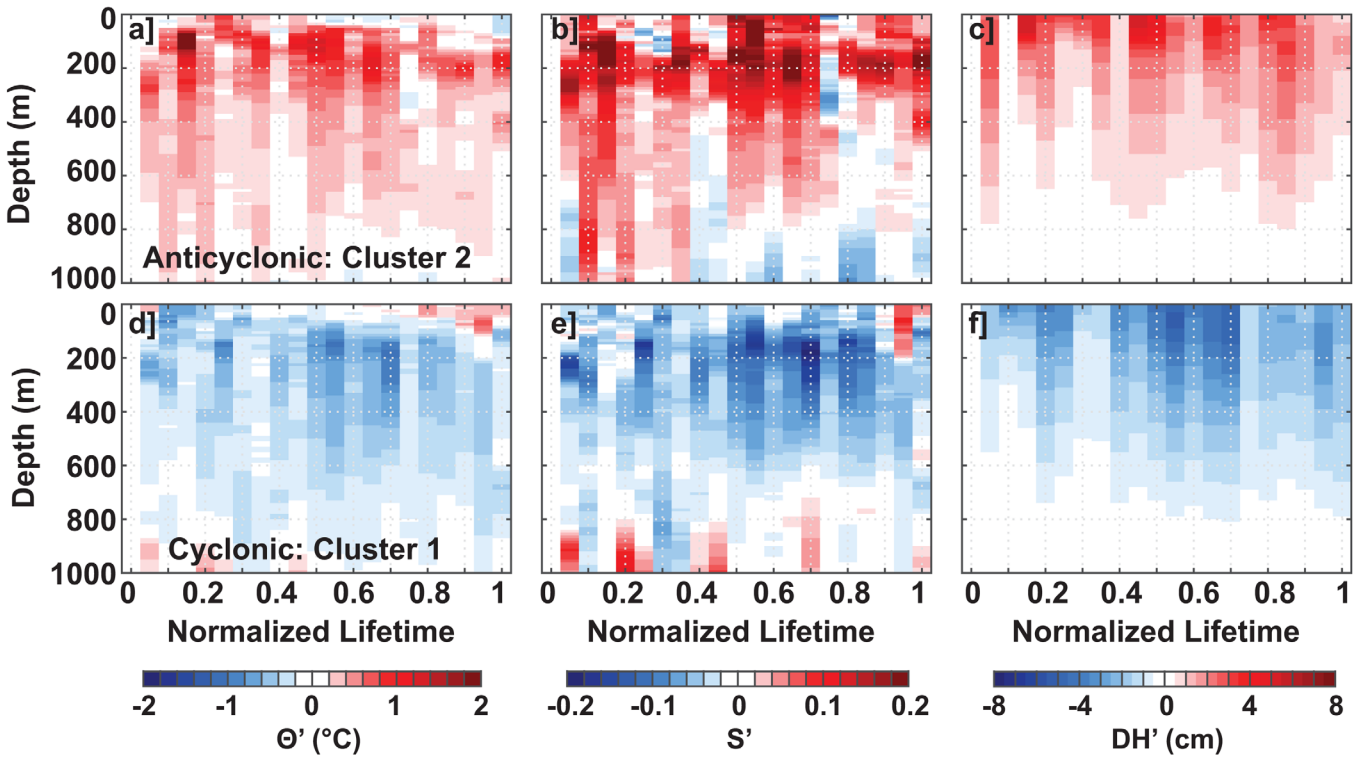

Figure 13. Same as Figure 7, but for the CANUS. (a–c) Cluster 2 of the AEs shown in Figure 11. (d–f) Cluster 1 of the CEs shown in Figure 12.

3.2.4. Benguela Upwelling System (BENUS)

The BENUS is the unique upwelling system where the clustering analysis suggests the presence of three main eddy-types, both for AEs and CEs (Figures 14 and 15). The first AE type regroups 55% of the trajectories and exhibits weak positive θ' of 0.3°C and S′ of 0.05 between the surface and ∼150 m depth (Figures 14b and 14c). On average, the corresponding DH′ is less than 1 cm (Figure 14d) and this cluster is thus associated with weakly surface-intensified eddies that are found all along the Namibian and South African coast (Figure 14a). The temporal evolution of this cluster is erratic (not shown), and confirms that these eddies are not significant despite the relatively large number of profiles and trajectories involved. The second cluster regroups 29% of the trajectories and is associated with relatively weak subsurface eddies, with a maximum θ' of 0.5°C and S′ of 0.07 between 250 and 500 m depth, (Figures 14f and 14g). These eddies, that have a marked signature on θ' and S′ down to 600–800 m depth, are associated with rather weak DH′ that is not clearly significant below 200–400 m depth (Figure 14h). These eddies are mainly formed along the Namibian coast in the Northern part of the BENUS (Figure 14e). The third eddy-type represents only 16% of the trajectories that are formed near the southwest tip of South Africa, in the southernmost part of the BENUS (Figure 14i). This cluster exhibits θ' and S′ of 1°C and 0.1 between 100 m and 800 m depth (Figures 14j and 14k). It is associated with highly significant DH′ above 800 m depth that reaches a maximum value of ∼6 cm at the sea-surface (Figure 14l). These subsurface-intensified AEs are thus very strong compared to the AEs of the other EBUS.

Figures 16a–16f show the composite temporal evolution of the eddy vertical structure for the second and third AE clusters. These evolution are consistent with their mean vertical profiles, and again the different phases are not clearly distinguishable (Figures 16a–16f). Although the growth phase was poorly sampled (less than 5% of the available profiles), the decay phase was much more sampled (∼22% of the available Argo profiles) but does not exhibit clear different patterns than the mature phase. For the third AE cluster, the strong subsurface-intensified eddies show significantly larger amplitude (7.5 cm) than the other eddy-types (3.0 cm for the first cluster and 3.7 cm for the second cluster).

The CEs of the BENUS exhibit similar but opposite patterns to the AEs. The first CEs type regroups 42% of the trajectories and shows very weak anomalies in the near-surface layers above the pycnocline, with

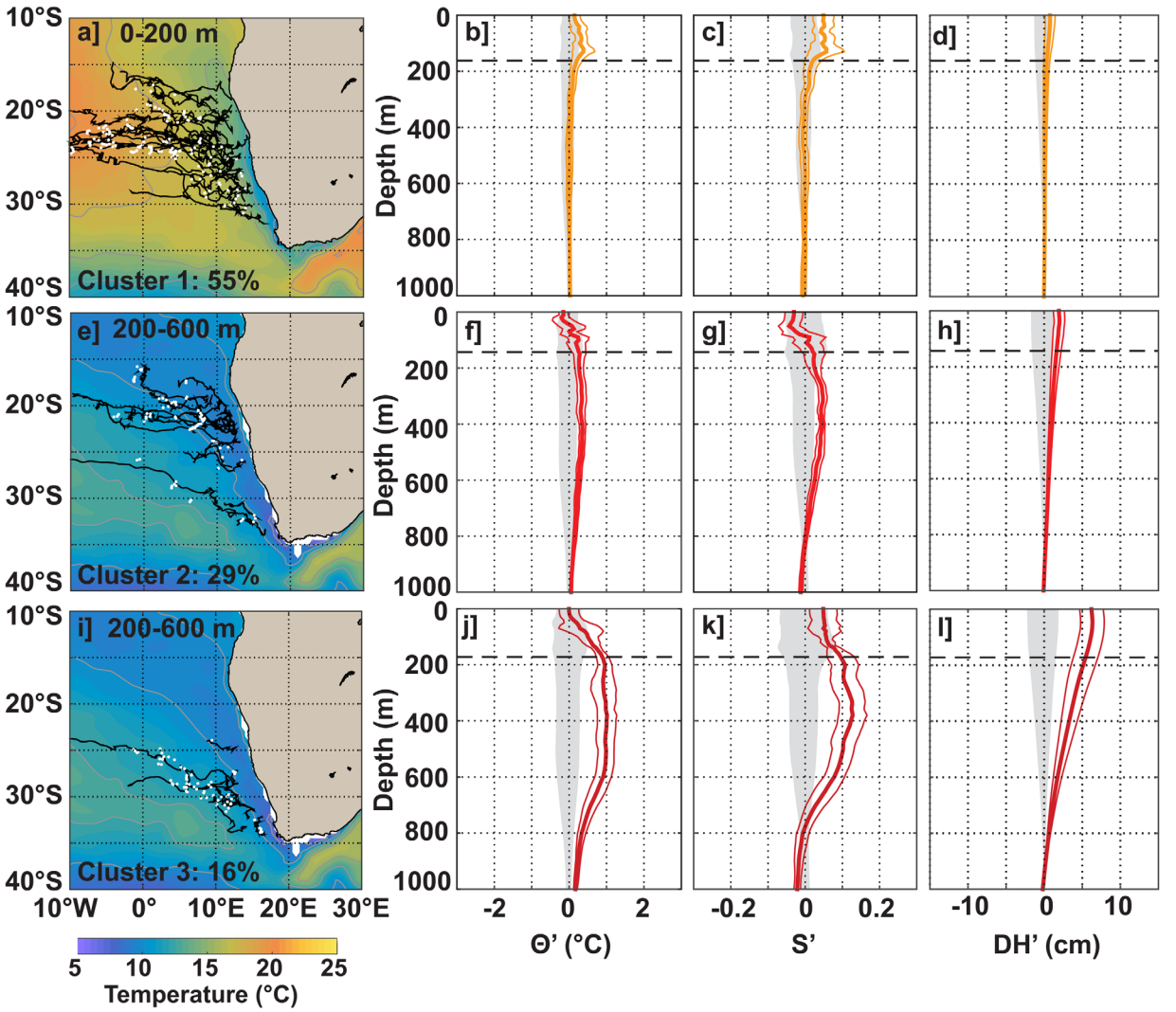

Figure 14. Same as Figure 5, but for the BENUS anticyclones. For this EBUS, the clustering analysis suggested the presence of three main AE-types and the scales have been changed to better highlight the mean anomaly profiles.

−0.3°C for θ', −0.05 for S′ (Figures 15b and 15c), and −1.5 cm for DH′ (Figure 15d). These surface-intensified eddies are mainly formed in the northern part of the BENUS, north of 27°N (Figure 15a). As for the AEs, the temporal evolution of this cluster is not homogeneous, with noisy and weak nonsignificant anomalies (not shown). The second CE type regroups 49% of the trajectories and corresponds to subsurface-intensified eddies that extends down to ∼800 m depth with maximum negative θ' (S′, respectively) of −0.8°C (−0.1) between 200 m and 600 m depth (Figures 15f and 15g). The associated DH′ reaches −5 cm at the sea-surface and is significant down to 600–800 m depth (Figure 15h). These eddies are found all along the BENUS coastline, with a higher generation south of 24°S (Figure 15e). The deep vertical extent of these CEs generated near the coast was previously noticed by *Rubio et al.* [2009] in a modeling study, highlighting the capability of cyclones to generate anomalies down to 1200 m depth. Despite the particular shape of the temperature and salinity anomalies of this cluster, the dynamic height anomaly is rather similar to those observed for CEs in the other EBUS. The anomalies associated with these eddies are homogeneous between 100 and 600 m depth all along their lifetime (Figures 16g–16i). Finally, the third cluster represents only 9% of the trajectories, but corresponds to strong subsurface-intensified CEs with maximum negative anomalies of −2.1°C in temperature and −0.24 in salinity (Figures 15j and 15k). The associated mean DH′ profile is also the most intense and reaches a maximum value of −13.5 cm at the sea-surface (Figure 15l). These eddies, that extend at least down to 1000 m depth, are exclusively formed in the southernmost part

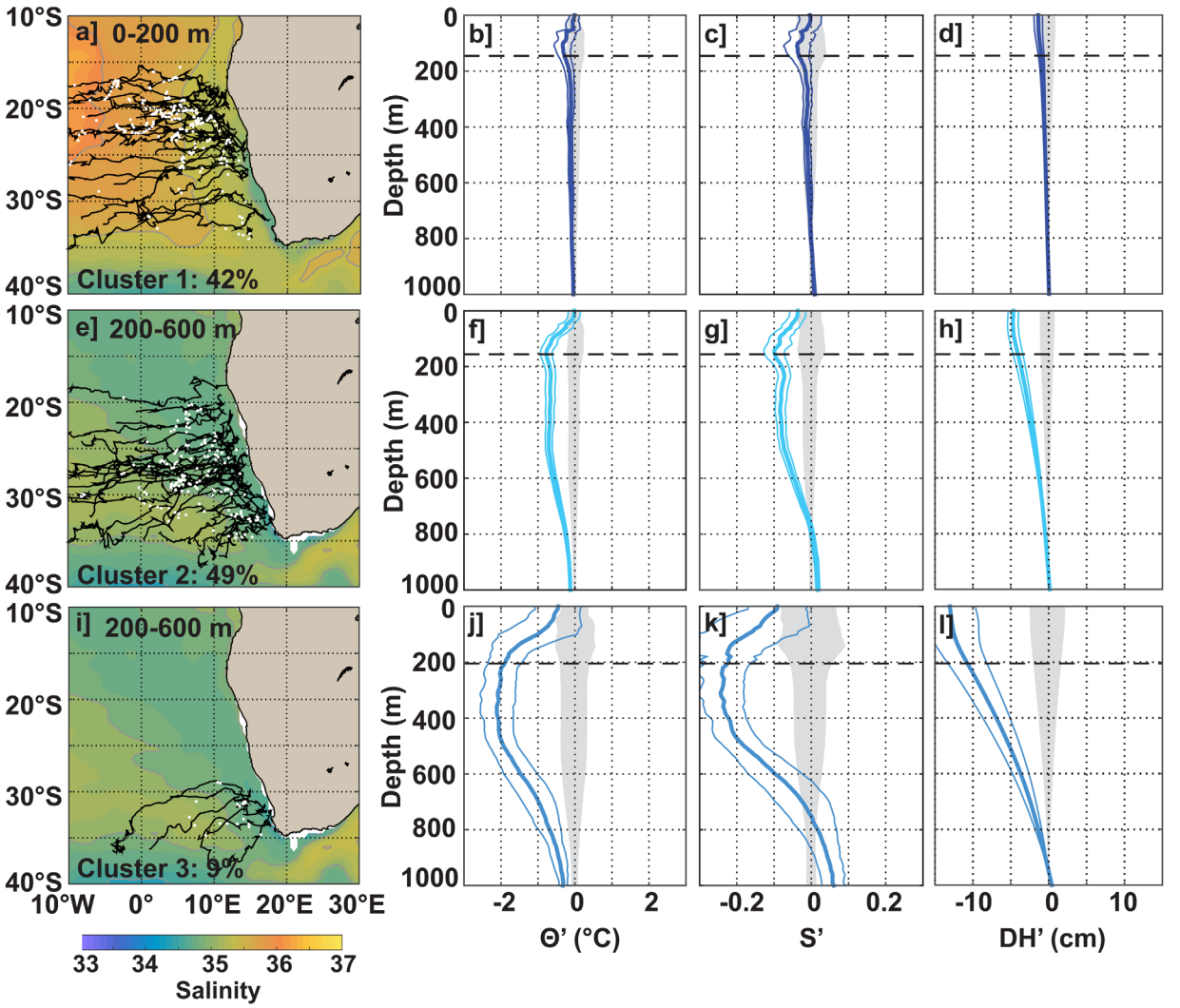

Figure 15. Same as Figure 6, but for the BENUS cyclones. For this EBUS, the clustering analysis suggested the presence of 3 main CE-types and the scales have been changed to better highlight the mean anomaly profiles.

of the BENUS, between 30°S and 34°S and propagate southwestward toward the Southern Ocean (Figure 15i). The temporal evolution of the strong subsurface-intensified anomalies of this cluster is also consistent with the mean vertical structure and does not show significant variations during the mature and decay phases (Figures 16j–16l). However, the limited number of collocated Argo profiles during the growth phase (less than 5% of the available profiles) prevent us to investigate the evolution at the beginning of the life-time. As for the strong subsurface-intensified AEs, these CEs show significantly larger SLA amplitude (10.5 cm) than the other eddy-types (4.4 cm and 6.7 cm for clusters 1 and 2, respectively).

The origins of the AEs and CEs in the BENUS have been less well documented than in the other EBUS. Most studies have concentrated on the largest eddies formed south of the BENUS, including the intense Agulhas AE Rings [e.g., *Lutjeharms and Van Ballegooyen*, 1988; *Arhan et al.*, 1999; *De Ruijter et al.*, 1999; *Dencausse et al.*, 2010] and the Cape Cauldron CEs [*Boebel et al.*, 2003]. The Agulhas Rings appear as strong anomalies in the sea surface height and impact the column water down to 1500 m depth with positive anomalies of temperature and salinity that can reach 6°C and 0.6, respectively [*Van Ballegooyen et al.*, 1994]. Since we selected eddies within a generation zone located close to the coast and north of 34°S, these Agulhas Rings should not contribute to our data set. Indeed, our AEs from the third cluster are all generated inshore of the climatological "eddy corridor" [*Garzoli and Gordon*, 1996], and propagate north-westward along the northern flank of this corridor (Figure 14i).

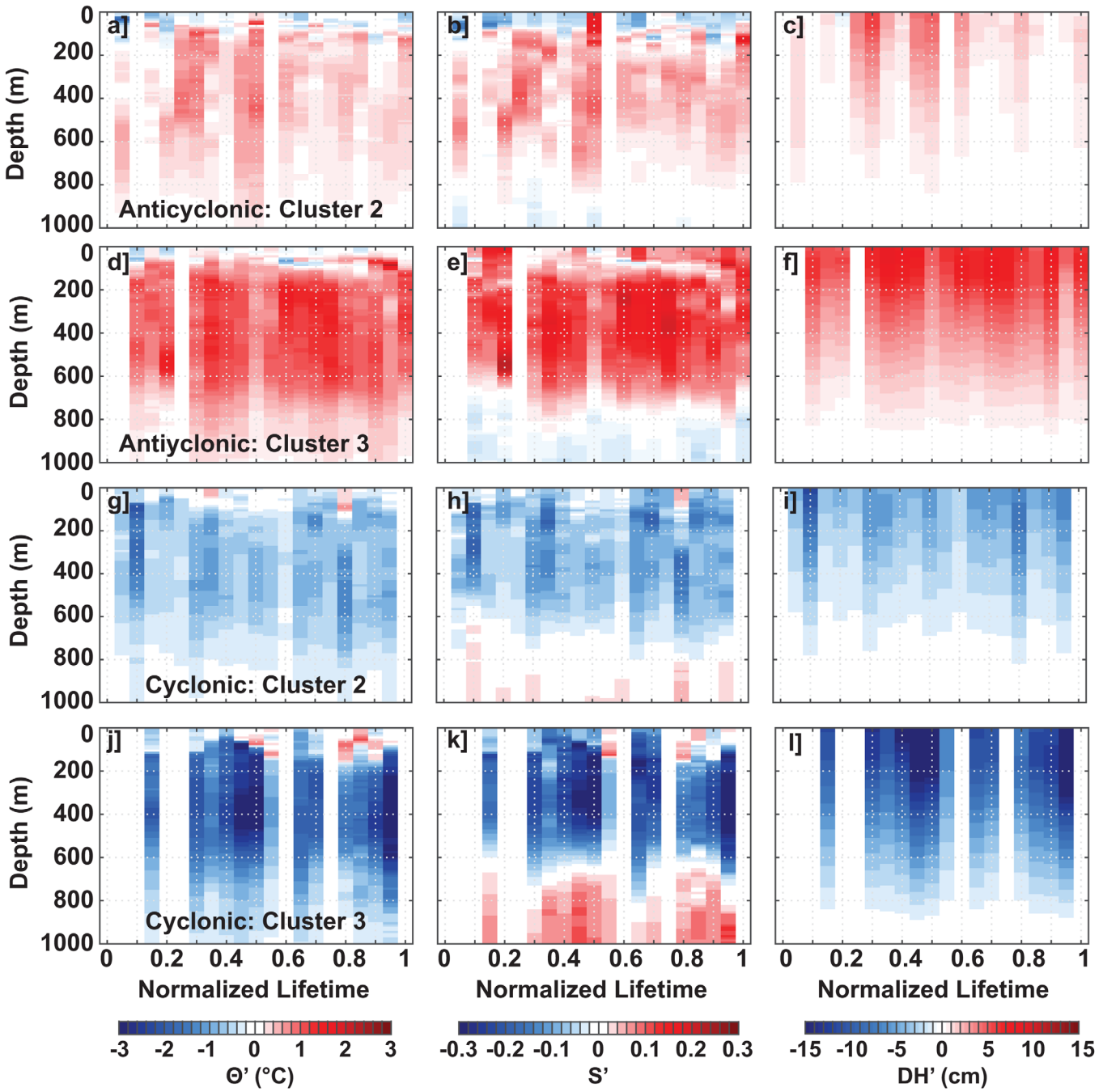

Figure 16. Same as Figure 7, but for the BENUS. (a–f) Clusters 2 and 3 of the AEs shown in Figure 14. (g-l) Clusters 2 and 3 of the CEs shown in Figure 15. Note that the scales have been changed to better highlight the temporal evolution of the anomalies.

More recently, some studies have highlighted the presence of cyclones associated with the Agulhas Rings in the Cape Cauldron region. The cyclones can have three main origins [*Boebel et al.*, 2003]. They can be generated in the Natal Pulse, on the east side of Africa [*Lutjeharms et al.*, 2003], or formed in the subantarctic zone and carrying subantarctic water [*Boebel et al.*, 2003], or composed of eddies generated at the shelf break on the west side of Africa, named "Cape Basin Cyclones." Only these latter cyclones can be generated north of 34°S near the coast, and can contribute to our set of CEs. Despite observational evidence of such cyclones in the Cape Cauldron area [*Boebel et al.*, 2003; *Richardson and Garzoli*, 2003; *Giulivi and Gordon*, 2006; *Lutjeharms*, 2006; *Richardson*, 2007; *Baker-Yeboah et al.*, 2010] and modeling studies [*Rubio et al.*, 2009;

Hall and Lutjeharms, 2011] the evolution of their vertical structure was not well understood. These CEs possibly originate from the destabilization of the along-shore current [*Shannon and Hunter*, 1988], from local upwelling along the shelf [*Shannon and Nelson*, 1996] or from Agulhas Rings interacting with the shelf [*Boebel et al*., 2003]. The strong local eddy-induced upwelling leads to negative temperature and salinity anomalies compared to anticyclones. A modeling study also simulated AEs generated along the coast, preferentially north of 26°S and slightly offshore compared to the CEs [*Rubio et al*., 2009].

Our analysis also shows that the subsurface eddies are generated in similar climatological background fields, although again the CEs tend to be formed closer to the coast where they may trap relatively cold and fresher water (Figures 14e, 14i, 15e, and 15i). Although difficult to observe with our data set, the local eddy-induced upwelling of isopycnals within CEs may amplify the strong initial negative θ' and S′; similarly, depression of isopycnals within AEs may amplify their initial positive θ' and S′. The subsurface CEs propagate west-southwestward, crossing the warm and salty tongue of Indian Ocean water entering the Atlantic Ocean, leading to greatly enhanced negative anomalies (Figure 15i). In contrast, the AEs generated slightly offshore trap relatively warmer and saltier water than the CEs, and then propagate in a less varying background, leading to anomalies with half the intensity of the CEs (Figure 14i). The second cluster, with weaker subsurface-intensified CEs and AEs, follows a similar pattern. The AEs are mainly generated north of 26°S whereas the CEs are formed preferentially south of 24°S. The upwelled water near the coast is warmer and saltier in the northern part of the BENUS, and the AE-cores show less difference compared to the background field than the CEs. Moreover, the CEs formed in the northern BENUS still propagate west-southwestward, crossing the warm and salty water corridor in the south of the region, maintaining their negative anomalies. The differences between the strong subsurface-intensified, high amplitude eddies and the relatively weaker surface-intensified ones appears to be mainly driven by their latitudinal generating location.

4. Discussion

Eddy vertical structure and their associated θ', S′ and DH′ are closely related to the water trapped in their cores at the beginning of their lifetime, but also to the eddy-induced upwelling or downwelling and to the evolution of the background θ/S fields they cross during their westward propagation. Even if the eddies are not particularly strong, they still contribute to the ocean internal mixing over smaller scales.

4.1. Pacific and Atlantic EBUS: Differences Between Their Respective Eddies

The different CE and AE types determined from a clustering analysis (HAC) of the Argo floats surfacing within eddies presented interesting characteristics. For the PCUS and the CALUS in the Pacific basin, the observed eddy-types were close to those previously documented. In both of these upwelling systems, the presence of strong subsurface-intensified anticyclones, carrying warm and salty water from their near-coastal poleward undercurrents, are well sampled by the Argo floats and match the previous observations [*Simpson et al*., 1984; *Johnson and McTaggart*, 2010; *Chaigneau et al*., 2011; *Kurian et al*., 2011; *Colas et al*., 2012; *Collins et al*., 2013]. However, we also highlighted the presence of weak surface-intensified anticyclones in the PCUS that represent 45% of the sampled eddies. To the best of our knowledge, these eddies as well as the quantification of the ratio of surface to subsurface-intensified eddies were not previously documented in this EBUS. Although they seem to be strongly influenced by air-sea interactions, and their anomalies are not strongly significant, their large number suggests that they may have a localized impact on physical and biogeochemical properties.

In contrast, the surface-intensified anticyclones of California are robust and may actively participate to the zonal redistribution of physical and bio-geochemical tracers over large distances from the coastal area to the open ocean [*Combes et al*., 2013]. The particularity of the surface-intensified eddies in the California Upwelling System is their mean S′, that shows a salty anomaly for CEs and a fresher anomaly for AEs, centered around the pycnocline depth, which is opposite to all the other EBUS. This strong S′ is likely due to the presence of the fresh Pacific Surface Water carried by the surface California Current, coupled with the eddy-induced upwelling or downwelling. The two CE-types of the CALUS have similar surface-intensified θ' as observed by *Kurian et al*. [2011] and unlike the PCUS, subsurface-intensified CEs are very rarely generated. Nevertheless, only *Chaigneau and Pizarro* [2005] has previously documented such a relative deep CE structure in the PCUS.

In the Atlantic EBUS, there are fewer results following the evolution of eddy properties over time, and our lagrangian average of the mean vertical structure of the AEs and CEs is quite new. Our study highlights that significant pycnocline-intensified eddies are generated all along the coast and in the lee of the Canary Islands, both for AEs and CEs. These CEs and AEs have similarly shaped vertical θ' and S′. Weaker eddies are mainly generated south of the Canary Island, where instabilities lead to the formation of numerous eddies [*Arístegui et al*., 1994; *Sangrà et al*., 2007, 2009]. Nevertheless, the majority of these weak eddies are robust enough to survive more than 30 days and propagate over large distances, thus may play a role on the mixing of tracers despite their nonsignificant anomalies.

Previous studies described the vertical structure of both cyclones and anticyclones formed in the lee of the Canary Islands, mainly generated by the destabilization of the Canary Current by the island topographic forcing and by the wind-induced upwelling at the western coast of the island or downwelling at the eastern part [*Pingree*, 1996; *Barton et al*., 2000; *Basterretxea et al*., 2002; *Piedeleu et al*., 2009]. For a long time, the Canary Islands were considered as the dominating generation area in the CANUS [*Sangrà et al*., 2009]. More recently, eddy formation was also linked to the destabilization of the fronts [*Meunier et al*., 2012] or coastal currents [*Meunier et al*., 2010; *Benítez-Barrios et al*., 2011; *Ruiz et al*., 2014]. Despite their different origins, the vertical structure of the eddies in these studies were quite similar, showing a core centered around 200 m depth, as in our study. Unlike the Pacific EBUS, where the vertical structure can be associated with a particular formation or behavior, the clusters of the CANUS may only separate stronger and weaker eddies. Nevertheless, more investigation is needed to understand the formation processes of these eddies, and the links between their amplitude, their evolution as they cross the background stratification, their isopycnal adjustment and their eddy-induced vertical movement.

The BENUS is rather unique, being the only upwelling system adjacent to a major inter-ocean exchange region—the Agulhas Indian-Atlantic region. This inter-ocean exchange contributes to a warm and salty tongue of water, extending offshore from where the BENUS eddies are generated in the coastal upwelling system. The influence of the warm, salty waters, both in the south and offshore, has many consequences for the BENUS eddies. Surface-intensified eddies are generated all along the coast, but we detect CEs closer to the coast in the cold, fresher upwelled waters, whereas the AEs are first detected further offshore, with warmer, saltier surface anomalies. The subsurface anomalies are generated all along the coast, but the strongest occur in the southern part of our domain. Although our generation region is chosen to be north of the Agulhas "eddy corridor," we may be detecting some remnants of the Agulhas Rings here, or instabilities trapping Agulhas water on the northern flank of this "corridor." Indeed, even the CEs may possibly originate from Agulhas Rings interacting with the shelf [*Boebel et al*., 2003]. The poleward propagation of the coastally formed CEs means they cross the warm, salty Agulhas outflow "corridor" which may contribute to their strong negative intensities. Indeed, on average satellite altimetry showed that CEs are larger and stronger than AEs (Figure 3). From the analysis of Argo floats we can further suggest that this difference is explained by the characteristics of the subsurface eddies: the subsurface CEs are much more energetic, exhibiting temperature, salinity, and dynamic height anomalies more than twice the anomalies associated with the subsurface AEs (Figures 14 and 15).

In this analysis, we found that the temporal evolution of the eddies' vertical structure does not evolve much over time. We have constructed composites of the mean vertical structure as a function of eddy lifetime, based on the Argo profiles for all eddies within the same cluster. Below the surface mixed layer, the θ' and S′ properties remained fairly constant, even during the generation and dissipation phases. This raises questions about the dynamics governing the observed changes in eddy amplitude and radius over time, based on altimetric analysis (Figure 3). If the upper ocean θ, S and DH anomalies are relatively constant on depth levels, the observed changes during the generation and dissipation phases may be due to other processes, such as the barotropic (or deeper baroclinic) adjustment of the eddies. However, this may also be a sampling issue, since the number of Argo profiles available in the generation and dissipation phases is also very limited.

4.2. Limitation of the Altimetry Maps and Argo Float Coverage

The merged analysis of SLA maps and Argo float profiles provides an unprecedented view of the vertical structure of AEs and CEs in the four EBUS. Even so, there are a number of limitations to the detection of these eddies using the available altimetry maps and Argo data. For instance, given the typical accuracy of satellite altimeter measurements [*Le Traon and Ogor*, 1998; *Chelton and Schlax*, 2003] and the spatial filtering applied

in the objective analysis used to produce SLA gridded maps [see *Chelton et al.*, 2011, Appendix A.3], eddies having an amplitude weaker than ~1–2 cm or a radius smaller than ~40 km should probably be considered as noisy artifact structures on the daily SLA maps. In this study, since we did not apply an amplitude or radius threshold in our eddy detection algorithm, such small and weak eddies have been detected. However, the tracking algorithm developed in this study eliminates the small random structures shorter than 30 days duration, and the remaining small-scale structures are part of the life-cycle of the long-lived coherent eddies. Although on average (see Table 2), these long-lived eddies have an amplitude (radius, respectively) higher than 4 cm (80 km) and are thus associated with a relatively high signal-to-noise ratio, the amplitude (radius) is often of ~1 cm (~20 km) at the beginning and end of their life-cycle (see Figure 3). Also not quantified, we believe that our tracking algorithm, based on a contour-intersection method (see section 2.1), is well adapted to follow eddies in a coherent way compared to algorithms based on distance criteria [e.g., *Penven et al.*, 2005; *Chaigneau et al.*, 2008; 2009; *Sangrá et al.*, 2009; *Chelton et al.*, 2011]. Our algorithm is an improved version of the fixed SLA contour algorithms, used to track eddies on weekly SLA maps in previous studies [e.g., *Fang and Morrow*, 2003; *Wang et al.*, 2003; *Hwang et al.*, 2004; *Morrow et al.*, 2004; *Chaigneau and Pizarro*, 2005].

In addition, Table 1 highlights the strong difference in the total number of Argo float profiles available in the four EBUS. Even in well covered zones such as the CALUS, we still observe some places where no Argo floats surfaced during the 10 years of data we analyzed (not shown). The BENUS is the least well-sampled system, especially North of 18°S, which has an impact on the representation of the sampled eddies. Table 2 shows that the eddies sampled by Argo floats exhibit larger radii and amplitudes, and longer lifetimes than the total set of long-lived eddies generated in the four major EBUS. It suggests that Argo floats surface preferentially in intense eddies and allow a robust description of the temporal evolution of the vertical structure of such eddies. This could be a sampling effect since larger eddies occupy more space and the Argo floats have statistically more chance to surface within larger surface-intensified eddies. More likely, this bias may be impacted by the eddy physics. Argo floats, whose parking depths are commonly between 500 m and 1000 m depth, are less likely to be trapped within surface-intensified eddies whose cores only extend down to ~200 m depth. Whereas if the core of the subsurface-intensified eddies reaches the Argo parking depths, then the floats can remain trapped in the eddies. The stronger the eddy, the stronger its vorticity and trapping effect. Indeed, some floats analyzed in this study remained trapped for several months in a few subsurface eddies. Since the larger and stronger eddies are more likely to be sampled by Argo floats, the composite evolution of the vertical structure can be biased by the occurrence of some intense eddies, as shown for instance for the subsurface-intensified AEs of the CALUS (Figures 10a–10c). It would be interesting to simulate the behavior of Argo floats at the vicinity of intense CEs and AEs, as well as weaker eddies, to study the mechanisms leading to the trapping of floats by eddies as a function of the eddy depth, velocity, radius and rotating sense.

Even though a larger number of floats sampled surface-intensified eddies, their mean vertical structure is closer to the random error estimate based on the profiles surfacing outside eddies, suggesting that these eddies may contribute less to the heat and salt exchange between the coast and the open ocean. Moreover, despite the effort made to sample more of the global ocean, we still do not have enough Argo floats at the beginning and the end of the eddy lifetime to robustly describe their generating and dissipation phases.

It is also important to bear in mind that the mean vertical structures presented here were obtained independently of the distance of the Argo floats from the eddy centers. For each of the clusters, the mean normalized distance of the floats from the eddy center to the eddy edge is around 50–75%. The mean value for the 4 EBUS is of 65%, very close to the theoretical value of 66.7% if we consider that the Argo floats are on average statistically evenly distributed over eddies of unit radius [*Chaigneau and Pizarro*, 2005]. First, this excellent agreement confirms that the eddy detection algorithm correctly identifies the eddy edge; a more restricted algorithm, based for instance on the maximum of swirl velocity [e.g., *Nencioli et al.*, 2010; *Liu et al.*, 2012] would decrease the eddy radius and positioned the Argo floats closer to the eddy edge or even outside the eddies. This would strongly limit the kind of analysis proposed in this study. Second, a mean normalized distance of 65% indicates that the anomalies shown in Figures 5–16 are more representative of the outer eddy vertical structure than the eddy center. Although anomalies are expected to be stronger at the eddy center, our limited data set could not be used to study the tridimensional structure for each cluster. Future studies based on an extended data set of Argo profiles or high-resolution modeling could allow us to document the composite structure of each eddy-type observed in the EBUS. Finally, although the mean normalized distance is higher than 60% for all the clusters, it is around 50% for the strongest subsurface-

intensified AEs and CEs of the BENUS (Clusters 3 in Figures 14 and 15). This reaffirms that the strong subsurface eddies are more efficiently trapping Argo floats.

5. Conclusion

With the increasing number of eddy resolving ocean models available, we need a better description of the observed vertical structure of the mesoscale eddies to improve the model validation and parametrizations. Until now, studies of the physical characteristics of the propagating mesoscale eddies were mainly based on altimetry data, which provides a robust analysis of the surface evolution of the larger eddies. The thermohaline characteristics of the eddies have been investigated locally, but regional studies have been limited by the coarse coverage of in situ data. In this study, we applied a tracking algorithm to altimetric maps to follow the eddies in time and space, and then collocated Argo floats to analyze their mean vertical and time-varying temperature, salinity and dynamic height anomalies. We applied a clustering technique, which allowed the reconstruction of the mean and temporal evolution of the vertical structure of eddies with similar temperature and salinity anomalies. When carefully separated, we were able to characterize the vertical structure of the surface and subsurface-intensified eddies in a lagrangian sense across the different EBUS. Although the surface signature of the AEs and CEs is comparable from one EBUS to another, their vertical thermohaline structure is quite distinct. The eddies' vertical structure depends on several factors such as *i)* the structure of the coastal current systems which generate instabilities, *ii)* the background climatological fields crossed by the eddies as they propagate into the ocean interior, *iii)* the ocean-atmosphere interactions in the surface layers and *iv)* the eddy-induced upwelling/downwelling within their core. In general, the vertical structure of the temperature, salinity and dynamic height anomalies remains quite stable along the eddies' lifetime. The surface eddies in most EBUS are warm, salty AEs and cold, fresh CEs, except for the CALUS in an exceptionally fresh surface regime, having warm, fresh AEs and cold, salty CEs. The strongest subsurface eddies occur in the BENUS, with intense AEs and CEs being impacted by the presence of the Agulhas water masses, and anomalies reaching 800 m depth on average.

Although we proposed some explanations for the eddy characteristics in each local formation region, further investigation is needed to better understand the theoretical mechanisms responsible for the formation of these mesoscale features and their temporal evolution. This work has concentrated on eddies formed in the near-coastal part of the EBUS only, a logical extension would be to analyze all of the eddies detected in the eastern boundary upwelling regions, including those formed outside the coastal area, for example, the Agulhas Rings and Cyclones, the "Mediterranean eddies" (Meddies) that can cross the offshore area of the Northern CANUS, and the eddies generated further offshore of the near-coastal EBUS.

Acknowledgments

Float data used here were collected and made freely available by Argo (http://www.argo.net/), a program of the Global Ocean Observing System, and contributing national programs. The altimeter products were produced by Ssalto/Duacs and distributed by AVISO, with support from CNES. Several Argo float deployments in the Peru-Chile Upwelling Systems have been supported by GMMC (Mercator-Coriolis) through the FLOPS (FLOtteurs du Pacifique Sud) project. C. Pegliasco was supported through a PhD grant from the *Direction Générale des Armées* (DGA, France). This work is a contribution to the LMI "Dynamiques du Système du Courant de Humboldt" (DISCOH) and the joint CNES/NASA OSTST project "*Merging of satellite and in situ observations for the analysis of meso and submesoscale dynamics*." We thank Y. Morel for his helpful discussion during the preparation of this manuscript. We thank D. Chelton and an anonymous reviewer for their very constructive comments to improve the manuscript.

References

Arhan, M., H. Mercier, and J. R. E. Lutjeharms (1999), The disparate evolution of three Agulhas rings in the South Atlantic Ocean, *J. Geophys. Res.*, *104*(C9), 20,987–21,005, doi:10.1029/1998JC900047.

Arístegui, J., P. Sangrá, S. Hernández-León, M. Cantón, A. Hernández-Guerra, and J. L. Kerling (1994), Island-induced eddies in the Canary islands, *Deep Sea Res., Part I*, *41*(10), 1509–1525, doi:10.1016/0967-0637(94)90058-2.

Arístegui, J., et al. (1997), The influence of island-generated eddies on chlorophyll distribution: A study of mesoscale variation around Gran Canaria, *Deep Sea Res., Part I*, *44*(1), 71–96, doi:10.1016/S0967-0637(96)00093-3.

Arístegui, J., E. D. Barton, X. A. Álvarez-Salgado, A. M. P. Santos, F. G. Figueiras, S. Kifani, S. Hernández-León, E. Mason, E. Machú, and H. Demarcq (2009), Sub-regional ecosystem variability in the Canary Current upwelling, *Prog. Oceanogr.*, *83*(1–4), 33–48, doi:10.1016/j.pocean.2009.07.031.

Baker-Yeboah, S., D. A. Byrne, and D. R. Watts (2010), Observations of mesoscale eddies in the South Atlantic Cape Basin: Baroclinic and deep barotropic eddy variability, *J. Geophys. Res.*, *115*, C12069, doi:10.1029/2010JC006236.

Bakun, A., and C. S. Nelson (1991), The Seasonal Cycle of Wind-Stress Curl in Subtropical Eastern Boundary Current Regions, *J. Phys. Oceanogr.*, *21*(12), 1815–1834, doi:10.1175/1520-0485(1991)021<1815:TSCOWS>2.0.CO;2.

Barton, E. D., and J. Arístegui (2004), The Canary Islands coastal transition zone—Upwelling, eddies and filaments, *Prog. Oceanogr.*, *62*(2–4), 67–69, doi:10.1016/j.pocean.2004.08.003.

Barton, E. D., et al. (1998), The transition zone of the Canary Current upwelling region, *Prog. Oceanogr.*, *41*(4), 455–504, doi:10.1016/S0079–6611(98)00023-8.

Barton, E. D., G. Basterretxea, P. Flament, E. G. Mitchelson-Jacob, B. Jones, J. Arístegui, and F. Herrera (2000), Lee region of Gran Canaria, *J. Geophys. Res.*, *105*(C7), 17,173–17,193, doi:10.1029/2000JC900010.

Basterretxea, G., E. D. Barton, P. Tett, P. Sangrá, E. Navarro-Perez, and J. Arístegui (2002), Eddy and deep chlorophyl maximum response to wind-shear in the lee of Gran Canaria, *Deep Sea Res., Part I*, *49*(6), 1087–1101, doi:10.1016/S0967-0637(02)00009-2.

Batteen, M. L., J. R. Martinez, D. W. Bryan, and E. J. Buch (2000), A modeling study of the coastal eastern boundary current system off Iberia and Morocco, *J. Geophys. Res.*, *105*(C6), 14,173–14,195, doi:10.1029/2000JC900026.

Batteen, M. L., N. J. Cipriano, and J. T. Monroe (2003), A large-scale seasonal modeling study of the California Current System, *J. Oceanogr.*, *59*(5), 545–562, doi:10.1023/B:JOCE.0000009585.24051.cc.

Benítez-Barrios, V. M., J. L. Pelegrí, A. Hernández-Guerra, K. M. M. Lwiza, D. Gomis, P. Vélez-Belchí, and S. Hernández-León (2011), Three-dimensional circulation in the NW Africa coastal transition zone, *Prog. Oceanogr.*, *91*(4), 516–533, doi:10.1016/j.pocean.2011.07.022.

Boebel, O., T. Rossby, J. Lutjeharms, W. Zenk, and C. Barron (2003), Path and variability of the Agulhas Return Current, *Deep Sea Res., Part II*, *50*(1), 35–56, doi:10.1016/S0967-0645(02)00377-6.

Capet, A., E. Mason, V. Rossi, C. Troupin, Y. Faugère, I. Pujol, and A. Pascual (2014), Implications of refined altimetry on estimates of mesoscale activity and eddy-driven offshore transport in the Eastern Boundary Upwelling Systems, *Geophys. Res. Lett.*, *41*, 7602–7610, doi:10.1002/2014GL061770.

Capet, X., F. Colas, J. C. Mcwilliams, P. Penven, and P. Marchesiello (2008), Eddies in Eastern Boundary Subtropical Upwelling Systems, in *Ocean Modeling in an Eddying Regime*, edited by M. W. Hecht and H. Hasumi, pp. 131–147, AGU, Washington, D. C.

Carr, M.-E., and E. J. Kearns (2003), Production regimes in four Eastern Boundary Current systems, *Deep Sea Res., Part II*, *50*(22–26), 3199–3221, doi:10.1016/j.dsr2.2003.07.015.

Castelao, R. M. (2014), Mesoscale eddies in the South Atlantic Bight and the Gulf Stream Recirculation region: Vertical structure, *J. Geophys. Res. Oceans*, *119*, 2048–2065, doi:10.1002/2014JC009796.

Chaigneau, A., and O. Pizarro (2005), Eddy characteristics in the eastern South Pacific, *J. Geophys. Res.*, *110*, C06005, doi:10.1029/2004JC002815.

Chaigneau, A., A. Gizolme, and C. Grados (2008), Mesoscale eddies off Peru in altimeter records: Identification algorithms and eddy spatio-temporal patterns, *Prog. Oceanogr.*, *79*(2–4), 106–119, doi:10.1016/j.pocean.2008.10.013.

Chaigneau, A., G. Eldin, and B. Dewitte (2009), Eddy activity in the four major upwelling systems from satellite altimetry (1992–2007), *Prog. Oceanogr.*, *83*(1–4), 117–123, doi:10.1016/j.pocean.2009.07.012.

Chaigneau, A., M. Le Texier, G. Eldin, C. Grados, and O. Pizarro (2011), Vertical structure of mesoscale eddies in the eastern South Pacific Ocean: A composite analysis from altimetry and Argo profiling floats, *J. Geophys. Res.*, *116*, C11025, doi:10.1029/2011JC007134.

Chaigneau, A., N. Dominguez, G. Eldin, L. Vasquez, R. Flores, C. Grados, and V. Echevin (2013), Near-coastal circulation in the Northern Humboldt Current System from shipboard ADCP data, *J. Geophys. Res. Oceans*, *118*, 5251–5266, doi:10.1002/jgrc.20328.

Chavez, F. P., and M. Messié (2009), A comparison of Eastern Boundary Upwelling Ecosystems, *Prog. Oceanogr.*, *83*(1–4), 80–96, doi:10.1016/j.pocean.2009.07.032.

Checkley, D. M., Jr., and J. A. Barth (2009), Patterns and processes in the California Current System, *Prog. Oceanogr.*, *83*(1–4), 49–64, doi:10.1016/j.pocean.2009.07.028.

Chelton, D. B., and M. G. Schlax (2003), The accuracies of smoothed sea surface height fields constructed from tandem satellite altimeter datasets, *J. Atmospheric Ocean. Technol.*, *20*(9), 1276–1302, doi:10.1175/1520-0426(2003)020<1276:TAOSSS>2.0.CO;2.

Chelton, D. B., M. G. Schlax, R. M. Samelson, and R. A. de Szoeke (2007), Global observations of large oceanic eddies, *Geophys. Res. Lett.*, *34*, L15606, doi:10.1029/2007GL030812.

Chelton, D. B., M. G. Schlax, and R. M. Samelson (2011), Global observations of nonlinear mesoscale eddies, *Prog. Oceanogr.*, *91*(2), 167–216, doi:10.1016/j.pocean.2011.01.002.

Chen, G., Y. Hou, and X. Chu (2011), Mesoscale eddies in the South China Sea: Mean properties, spatiotemporal variability, and impact on thermohaline structure, *J. Geophys. Res.*, *116*, C06018, doi:10.1029/2010JC006716.

Colas, F., J. C. McWilliams, X. Capet, and J. Kurian (2012), Heat balance and eddies in the Peru-Chile current system, *Clim. Dyn.*, *39*(1-2), 509–529, doi:10.1007/s00382-011-1170-6.

Collins, C. A., T. Margolina, T. A. Rago, and L. Ivanov (2013), Looping RAFOS floats in the California Current System, *Deep Sea Res., Part II*, *85*, 42–61, doi:10.1016/j.dsr2.2012.07.027.

Combes, V., F. Chenillat, E. Di Lorenzo, P. Rivière, M. D. Ohman, and S. J. Bograd (2013), Cross-shore transport variability in the California Current: Ekman upwelling vs. eddy dynamics, *Prog. Oceanogr.*, *109*, 78–89, doi:10.1016/j.pocean.2012.10.001.

Correa-Ramirez, M. A., S. Hormazábal, and G. Yuras (2007), Mesoscale eddies and high chlorophyll concentrations off central Chile (29°–39°S), *Geophys. Res. Lett.*, *34*, L12604, doi:10.1029/2007GL029541.

Cushman-Roisin, B., B. Tang, and E. P. Chassignet (1990), Westward motion of mesoscale eddies, *J. Phys. Oceanogr.*, *20*(5), 758–768, doi:10.1175/1520-0485(1990)020<0758:WMOME>2.0.CO;2.

Dencausse, G., M. Arhan, and S. Speich (2010), Routes of Agulhas rings in the southeastern Cape Basin, *Deep Sea Res., Part I*, *57*(11), 1406–1421, doi:10.1016/j.dsr.2010.07.008.

De Ruijter, W. P. M., A. Biastoch, S. S. Drijfhout, J. R. E. Lutjeharms, R. P. Matano, T. Pichevin, P. J. van Leeuwen, and W. Weijer (1999), Indian-Atlantic interocean exchange: Dynamics, estimation and impact, *J. Geophys. Res.*, *104*(C9), 20,885–20,910, doi:10.1029/1998JC900099.

Dong, C., X. Lin, Y. Liu, F. Nencioli, Y. Chao, Y. Guan, D. Chen, T. Dickey, and J. C. McWilliams (2012), Three-dimensional oceanic eddy analysis in the Southern California Bight from a numerical product, *J. Geophys. Res.*, *117*, C00H14, doi:10.1029/2011JC007354.

Dong, C., J. C. McWilliams, Y. Liu, and D. Chen (2014), Global heat and salt transports by eddy movement, *Nat. Commun.*, *5*, 1–6, doi:10.1038/ncomms4294.

Emery, W. J., and J. Meincke (1986), Global water masses-summary and review, *Oceanol. Acta*, *9*(4), 383–391.

Fang, F., and R. Morrow (2003), Evolution, movement and decay of warm-core Leeuwin Current eddies, *Deep Sea Res., Part II*, *50*(12–13), 2245–2261, doi:10.1016/S0967-0645(03)00055-9.

Frenger, I., N. Gruber, R. Knutti, and M. Münnich (2013), Imprint of Southern Ocean eddies on winds, clouds and rainfall, *Nat. Geosci.*, *6*(8), 608–612, doi:10.1038/ngeo1863.

Fréon, P., M. Barange, and J. Arístegui (2009), Eastern Boundary Upwelling Ecosystems: Integrative and comparative approaches, *Prog. Oceanogr.*, *83*(1–4), 1–14, doi:10.1016/j.pocean.2009.08.001.

Froyland, G., C. Horenkamp, V. Rossi, N. Santitissadeekorn, and A. S. Gupta (2012), Three-dimensional characterization and tracking of an Agulhas Ring, *Ocean Modell.*, *52–53*, 69–75, doi:10.1016/j.ocemod.2012.05.001.

Garfield, N., C. A. Collins, R. G. Paquette, and E. Carter (1999), Lagrangian exploration of the California Undercurrent, 1992–95, *J. Phys. Oceanogr.*, *29*(4), 560–583, doi:10.1175/1520-0485(1999)029<0560:LEOTCU>2.0.CO;2.

Garzoli, S. L., and A. L. Gordon (1996), Origins and variability of the Benguela Current, *J. Geophys. Res.*, *101*(C1), 897–906, doi:10.1029/95JC03221.

Garzoli, S. L., P. L. Richardson, C. M. D. Rae, D. M. Fratantoni, G. J. Goñi, and A. J. Roubicek (1999), Three Agulhas rings observed during the Benguela Current Experiment, *J. Geophys. Res.*, *104*(C9), 20,971–20,985, doi:10.1029/1999JC900060.

Giulivi, C. F., and A. L. Gordon (2006), Isopycnal displacements within the Cape Basin thermocline as revealed by the Hydrographic Data Archive, *Deep Sea Res., Part I*, *53*(8), 1285–1300, doi:10.1016/j.dsr.2006.05.011.

Gordon, A. L. (2003), Oceanography: The brawniest retroflection, *Nature*, *421*(6926), 904–905, doi:10.1038/421904a.

Gruber, N., Z. Lachkar, H. Frenzel, P. Marchesiello, M. Münnich, J. C. McWilliams, T. Nagai, and G.-K. Plattner (2011), Eddy-induced reduction of biological production in eastern boundary upwelling systems, *Nat. Geosci.*, *4*(11), 787–792, doi:10.1038/ngeo1273.

Hall, C., and J. R. E. Lutjeharms (2011), Cyclonic eddies identified in the Cape Basin of the South Atlantic Ocean, *J. Mar. Syst.*, *85*(1–2), 1–10, doi:10.1016/j.jmarsys.2010.10.003.

Hardman-Mountford, N. J., A. J. Richardson, J. J. Agenbag, E. Hagen, L. Nykjaer, F. A. Shillington, and C. Villacastin (2003), Ocean climate of the South East Atlantic observed from satellite data and wind models, *Prog. Oceanogr.*, *59*(2–3), 181–221, doi:10.1016/j.pocean.2003.10.001.

Holte, J., F. Straneo, C. Moffat, R. Weller, and J. T. Farrar (2013), Structure and surface properties of eddies in the southeast Pacific Ocean, *J. Geophys. Res. Oceans*, *118*, 2295–2309, doi:10.1002/jgrc.20175.

Hormazabal, S., V. Combes, C. E. Morales, M. A. Correa-Ramirez, E. Di Lorenzo, and S. Nuñez (2013), Intrathermocline eddies in the coastal transition zone off central Chile (31–41°S), *J. Geophys. Res. Oceans*, *118*, 4811–4821, doi:10.1002/jgrc.20337.

Hutchings, L., et al. (2009), The Benguela Current: An ecosystem of four components, *Prog. Oceanogr.*, *83*(1–4), 15–32, doi:10.1016/j.pocean.2009.07.046.

Huyer, A., P. M. Kosro, J. Fleischbein, S. R. Ramp, T. Stanton, L. Washburn, F. P. Chavez, T. J. Cowles, S. D. Pierce, and R. L. Smith (1991), Currents and water masses of the Coastal Transition Zone off northern California, June to August 1988, *J. Geophys. Res.*, *96*(C8), 14,809–14,831, doi:10.1029/91JC00641.

Huyer, A., J. A. Barth, P. M. Kosro, R. K. Shearman, and R. L. Smith (1998), Upper-ocean water mass characteristics of the California current, Summer 1993, *Deep Sea Res., Part II*, *45*(8–9), 1411–1442, doi:10.1016/S0967-0645(98)80002-7.

Hwang, C., C.-R. Wu, and R. Kao (2004), TOPEX/Poseidon observations of mesoscale eddies over the Subtropical Countercurrent: Kinematic characteristics of an anticyclonic eddy and a cyclonic eddy, *J. Geophys. Res.*, *109*, C08013, doi:10.1029/2003JC002026.

Jerónimo, G., and J. Gómez-Valdés (2007), A subsurface warm-eddy off northern Baja California in July 2004, *Geophys. Res. Lett.*, *34*, L06610, doi:10.1029/2006GL028851.

Johnson, G. C., and K. E. McTaggart (2010), Equatorial Pacific 13°C Water Eddies in the Eastern Subtropical South Pacific Ocean*, *J. Phys. Oceanogr.*, *40*(1), 226–236, doi:10.1175/2009JPO4287.1.

Kurczyn, J. A., E. Beier, M. F. Lavín, and A. Chaigneau (2012), Mesoscale eddies in the northeastern Pacific tropical-subtropical transition zone: Statistical characterization from satellite altimetry, *J. Geophys. Res.*, *117*, C10021, doi:10.1029/2012JC007970.

Kurian, J., F. Colas, X. Capet, J. C. McWilliams, and D. B. Chelton (2011), Eddy properties in the California Current System, *J. Geophys. Res.*, *116*, C08027, doi:10.1029/2010JC006895.

Le Traon, P.-Y., and F. Ogor (1998), ERS-1/2 orbit improvement using TOPEX/POSEIDON: The 2 cm challenge, *J. Geophys. Res.*, *103*, 8045–8057, doi:10.1029/97JC01917.

Liu, Y., C. Dong, Y. Guan, D. Chen, J. McWilliams, and F. Nencioli (2012), Eddy analysis in the subtropical zonal band of the North Pacific Ocean, *Deep Sea Res., Part I*, *68*, 54–67, doi:10.1016/j.dsr.2012.06.001.

Logerwell, E. A., and P. E. Smith (2001), Mesoscale eddies and survival of late stage Pacific sardine (Sardinops sagax) larvae, *Fish. Oceanogr.*, *10*(1), 13–25, doi:10.1046/j.1365-2419.2001.00152.x.

Lutjeharms, J. R. (2006), The Agulhas Current retroflection, *Agulhas Curr.*, 151–207.

Lutjeharms, J. R. E., and R. C. Van Ballegooyen (1988), The retroflection of the Agulhas Current, *J. Phys. Oceanogr.*, *18*(11), 1570–1583, doi:10.1175/1520-0485(1988)018<1570:TROTAC>2.0.CO;2.

Lutjeharms, J. R. E., P. Penven, and C. Roy (2003), Modelling the shear edge eddies of the southern Agulhas Current, *Cont. Shelf Res.*, *23*(11–13), 1099–1115, doi:10.1016/S0278-4343(03)00106-7.

Machín, F., A. Hernández-Guerra, and J. L. Pelegrí (2006), Mass fluxes in the Canary Basin, *Prog. Oceanogr.*, *70*(2–4), 416–447, doi:10.1016/j.pocean.2006.03.019.

Mahadevan, A. (2014), Ocean science: Eddy effects on biogeochemistry, *Nature*, *506*(7487), 168–169, doi:10.1038/nature13048.

Marchesiello, P., and P. Estrade (2007), Eddy activity and mixing in upwelling systems: A comparative study of Northwest Africa and California regions, *Int. J. Earth Sci.*, *98*(2), 299–308, doi:10.1007/s00531-007-0235-6.

Meunier, T., V. Rossi, Y. Morel, and X. Carton (2010), Influence of bottom topography on an upwelling current: Generation of long trapped filaments, *Ocean Modell.*, *35*(4), 277–303, doi:10.1016/j.ocemod.2010.08.004.

Meunier, T., E. D. Barton, B. Barreiro, and R. Torres (2012), Upwelling filaments off Cap Blanc: Interaction of the NW African upwelling current and the Cape Verde frontal zone eddy field?, *J. Geophys. Res.*, *117*, C08031, doi:10.1029/2012JC007905.

Mittelstaedt, E. (1983), The upwelling area off Northwest Africa—A description of phenomena related to coastal upwelling, *Prog. Oceanogr.*, *12*(3), 307–331, doi:10.1016/0079–6611(83)90012-5.

Montes, I., F. Colas, X. Capet, and W. Schneider (2010), On the pathways of the equatorial subsurface currents in the eastern equatorial Pacific and their contributions to the Peru-Chile Undercurrent, *J. Geophys. Res.*, *115*, C09003, doi:10.1029/2009JC005710.

Morales, C. E., S. Hormazabal, M. Correa-Ramirez, O. Pizarro, N. Silva, C. Fernandez, V. Anabalón, and M. L. Torreblanca (2012), Mesoscale variability and nutrient–phytoplankton distributions off central-southern Chile during the upwelling season: The influence of mesoscale eddies, *Prog. Oceanogr.*, *104*, 17–29, doi:10.1016/j.pocean.2012.04.015.

Morrow, R., and P.-Y. Le Traon (2012), Recent advances in observing mesoscale ocean dynamics with satellite altimetry, *Adv. Space Res.*, *50*(8), 1062–1076, doi:10.1016/j.asr.2011.09.033.

Morrow, R., F. Birol, D. Griffin, and J. Sudre (2004), Divergent pathways of cyclonic and anti-cyclonic ocean eddies, *Geophys. Res. Lett.*, *31*, L24311, doi:10.1029/2004GL020974.

Nencioli, F., C. Dong, T. Dickey, L. Washburn, and J. C. McWilliams (2010), A vector geometry–based eddy detection algorithm and its application to a high-resolution numerical model product and high-frequency radar surface velocities in the Southern California Bight, *J. Atmos. Oceanic Technol.*, *27*(3), 564–579, doi:10.1175/2009JTECHO725.1.

Pacheco, M. M., and A. Hernandez-Guerra (1999), Seasonal variability of recurrent phytoplankton pigment patterns in the Canary Islands area, *Int. J. Remote Sens.*, *20*(7), 1405–1418, doi:10.1080/014311699212795.

Paillet, J., B. Le Cann, X. Carton, Y. Morel, and A. Serpette (2002), Dynamics and evolution of a Northern Meddy, *J. Phys. Oceanogr.*, *32*(1), 55–79, doi:10.1175/1520-0485(2002)032<0055:DAEOAN>2.0.CO;2.

Pauly, D., and V. Christensen (1995), Primary production required to sustain global fisheries, *Nature*, *374*(6519), 255–257, doi:10.1038/374255a0.

Pelland, N. A., C. C. Eriksen, and C. M. Lee (2013), Subthermocline Eddies over the Washington Continental Slope as Observed by Seagliders, 2003–09, *J. Phys. Oceanogr.*, *43*(10), 2025–2053, doi:10.1175/JPO-D-12–086.1.

Penven, P., V. Echevin, J. Pasapera, F. Colas, and J. Tam (2005), Average circulation, seasonal cycle, and mesoscale dynamics of the Peru Current System: A modeling approach, *J. Geophys. Res.*, *110*, C10021, doi:10.1029/2005JC002945.

Piedeleu, M., P. Sangrà, A. Sánchez-Vidal, J. Fabrés, C. Gordo, and A. Calafat (2009), An observational study of oceanic eddy generation mechanisms by tall deep-water islands (Gran Canaria), *Geophys. Res. Lett.*, *36*, L14605, doi:10.1029/2008GL037010.

Pierce, S. D., R. L. Smith, P. M. Kosro, J. A. Barth, and C. D. Wilson (2000), Continuity of the poleward undercurrent along the eastern boundary of the mid-latitude north Pacific, *Deep Sea Res., Part II*, *47*(5–6), 811–829, doi:10.1016/S0967-0645(99)00128-9.

Pietri, A., P. Testor, V. Echevin, A. Chaigneau, L. Mortier, G. Eldin, and C. Grados (2012), Finescale vertical structure of the upwelling system off Southern Peru as observed from glider data, *J. Phys. Oceanogr.*, *43*(3), 631–646, doi:10.1175/JPO-D-12-035.1.

Pietri, A., V. Echevin, P. Testor, A. Chaigneau, L. Mortier, C. Grados, and A. Albert (2014), Impact of a coastal-trapped wave on the near-coastal circulation of the Peru upwelling system from glider data, *J. Geophys. Res. Oceans*, *119*, 2109–2120, doi:10.1002/2013JC009270.

Pingree, R. D. (1996), A shallow subtropical subducting westward propagating eddy (Swesty), *Philos. Trans. R. Soc. London A*, *354*(1710), 979–1026, doi:10.1098/rsta.1996.0039.

Richardson, P., and S. Garzoli (2003), Characteristics of intermediate water flow in the Benguela current as measured with RAFOS floats, *Deep Sea Res., Part II*, *50*(1), 87–118, doi:10.1016/S0967-0645(02)00380-6.

Richardson, P. L. (2007), Agulhas leakage into the Atlantic estimated with subsurface floats and surface drifters, *Deep Sea Res., Part I*, *54*(8), 1361–1389, doi:10.1016/j.dsr.2007.04.010.

Roux, M. (1985), *Algorithmes de Classification*, Masson, Paris.

Rubio, A., B. Blanke, S. Speich, N. Grima, and C. Roy (2009), Mesoscale eddy activity in the southern Benguela upwelling system from satellite altimetry and model data, *Prog. Oceanogr.*, *83*(1–4), 288–295, doi:10.1016/j.pocean.2009.07.029.

Ruiz, S., J. L. Pelegrí, M. Emelianov, A. Pascual, and E. Mason (2014), Geostrophic and ageostrophic circulation of a shallow anticyclonic eddy off Cape Bojador, *J. Geophys. Res. Oceans*, *119*, 1257–1270, doi:10.1002/2013JC009169.

Samelson, R. M., M. G. Schlax, and D. B. Chelton (2014), Randomness, symmetry, and scaling of mesoscale eddy life cycles, *J. Phys. Oceanogr.*, *44*(3), 1012–1029, doi:10.1175/JPO-D-13–0161.1.

Sangrà, P., M. Auladell, A. Marrero-Díaz, J. L. Pelegrí, E. Fraile-Nuez, A. Rodríguez-Santana, J. M. Martín, E. Mason, and A. Hernández-Guerra (2007), On the nature of oceanic eddies shed by the Island of Gran Canaria, *Deep Sea Res., Part I*, *54*(5), 687–709, doi:10.1016/j.dsr.2007.02.004.

Sangrà, P., et al. (2009), The Canary Eddy Corridor: A major pathway for long-lived eddies in the subtropical North Atlantic, *Deep Sea Res., Part I*, *56*(12), 2100–2114, doi:10.1016/j.dsr.2009.08.008.

Schneider, W., R. Fuenzalida, E. Rodríguez-Rubio, J. Garcés-Vargas, and L. Bravo (2003), Characteristics and formation of Eastern South Pacific Intermediate Water, *Geophys. Res. Lett.*, *30*(11), 1581, doi:10.1029/2003GL017086.

Shannon, L. V., and D. Hunter (1988), Notes on Antarctic intermediate water around southern Africa, *South Afr. J. Mar. Sci.*, *6*(1), 107–117, doi:10.2989/025776188784480735.

Shannon, L. V., and G. Nelson (1996), The Benguela: Large scale features and processes and system variability, in *The South Atlantic*, pp. 163–210, Springer, Berlin.

Shillington, F. A., C. J. C. Reason, C. M. Duncombe Rae, P. Florenchie, and P. Penven (2006), 4 Large scale physical variability of the Benguela Current Large Marine Ecosystem (BCLME), in *Large Marine Ecosystems*, vol. 14, edited by G. H. Vere Shannon, pp. 49–70, Elsevier, Oxford, U. K.

Silva, N., and S. Neshyba (1979), On the southernmost extension of the Peru-Chile undercurrent, *Deep Sea Res., Part I*, *26*(12), 1387–1393, doi:10.1016/0198-0149(79)90006-2.

Silva, N., N. Rojas, and A. Fedele (2009), Water masses in the Humboldt Current System: Properties, distribution, and the nitrate deficit as a chemical water mass tracer for Equatorial Subsurface Water off Chile, *Deep Sea Res., Part II*, *56*(16), 1004–1020, doi:10.1016/j.dsr2.2008.12.013.

Simpson, J. J., and R. J. Lynn (1990), A mesoscale eddy dipole in the offshore California Current, *J. Geophys. Res.*, *95*(C8), 13,009–13,022, doi:10.1029/JC095iC08p13009.

Simpson, J. J., T. D. Dickey, and C. J. Koblinsky (1984), An offshore eddy in the California current system Part I: Interior dynamics, *Prog. Oceanogr.*, *13*(1), 5–49, doi:10.1016/0079–6611(84)90004-1.

Souza, J. M. A. C., C. de Boyer Montégut, and P. Y. Le Traon (2011), Comparison between three implementations of automatic identification algorithms for the quantification and characterization of mesoscale eddies in the South Atlantic Ocean, *Ocean Sci. Discuss.*, *8*(2), 483–531, doi:10.5194/osd-8–483-2011.

Stramma, L., H. W. Bange, R. Czeschel, A. Lorenzo, and M. Frank (2013), On the role of mesoscale eddies for the biological productivity and biogeochemistry in the eastern tropical Pacific Ocean off Peru, *Biogeosciences*, *10*(11), 7293–7306, doi:10.5194/bg-10-7293-2013.

Strub, P. T., J. M. Mesias, V. Montecino, J. Rutland, and S. Salinas (1998), Coastal Ocean Circulation off Western South America, in The Sea, vol. 11, edited by A. R. Robinson, and K. H. Brink, pp. 273–313, John Wiley and Sons, Hoboken, N. J.

Strub, P. T., V. Combes, F. Shilington, and O. Pizarro (2013), Currents and processes along the Eastern Boundaries, in *Ocean Circulation and Climate: A 21st Century Perspective*, edited by G. Siedler, et al., pp. 339–384, Elsevier Ltd., Oxford, U. K.

Tomczak, M., and J. S. Godfrey (1994), *Regional Oceanography: an Introduction*, Elsevier Sci. Ltd., Oxford, U. K.

Van Ballegooyen, R. C., M. L. Gründlingh, and J. R. E. Lutjeharms (1994), Eddy fluxes of heat and salt from the southwest Indian Ocean into the southeast Atlantic Ocean: A case study, *J. Geophys. Res.*, *99*(C7), 14,053–14,070, doi:10.1029/94JC00383.

Villas Bôas, A. B., O. T. Sato, A. Chaigneau, and G. P. Castelão (2015), The signature of mesoscale eddies on the air-sea turbulent heat fluxes in the South Atlantic Ocean, *Geophys. Res. Lett.*, *42*, 1856–1862, doi:10.1002/2015GL063105.

Wang, G., J. Su, and P. C. Chu (2003), Mesoscale eddies in the South China Sea observed with altimeter data, *Geophys. Res. Lett.*, *30*(21), 2121, doi:10.1029/2003GL018532.

Ward, J. H. (1963), Hierarchical grouping to optimize an objective function, *J. Am. Stat. Assoc.*, *58*(301), 236–244, doi:10.1080/01621459.1963.10500845.

Yang, G., F. Wang, Y. Li, and P. Lin (2013), Mesoscale eddies in the northwestern subtropical Pacific Ocean: Statistical characteristics and three-dimensional structures, *J. Geophys. Res. Oceans*, *118*, 1906–1925, doi:10.1002/jgrc.20164.

Yi, J., Y. Du, Z. He, and C. Zhou (2014), Enhancing the accuracy of automatic eddy detection and the capability of recognizing the multi-core structures from maps of sea level anomaly, *Ocean Sci*, *10*(1), 39–48, doi:10.5194/os-10-39-2014.